Mycobacterium tuberculosis partitions the Krebs cycle to persist under iron starvation.

Agnese Serafini[a,1], Acely Garza-Garcia[b], Davide Sorze[a], Luiz Pedro Sorio de Carvalho[b,c], and Riccardo Manganelli[a].

[a]Department of Molecular Medicine, University of Padova, Via A. Gabelli 63, Padova 35121, Italy.

[b]Mycobacterial Metabolism and Antibiotic Research Laboratory, The Francis Crick Institute, 1 Midland Rd, London NW1 1AT, UK.

[c]Chemistry Department, The Herbert Wertheim UF Scripps Institute for Biomedical Innovation & Technology, 120 Scripps Way, Jupiter, FL 33458, USA.

[1]To whom correspondence should be addressed. Email: agnese.serafini@unipd.it

iron starvation | *Mycobacterium tuberculosis* | central carbon metabolism | isotope tracing | nutritional immunity |

Abstract

In this study, we investigated how iron limitation alters central metabolism in *Mycobacterium tuberculosis* using metabolomics and stable isotope tracing. Our findings reveal a well-orchestrated metabolic program to enable Krebs cycle activity despite the inefficient action of its iron-dependent enzymes. Under such conditions, carbon flux through the oxidative branch of the Krebs cycle is stalled, resulting in the accumulation of metabolites that are partially secreted. As a result, carbon flux from glycolysis is partially diverted to the reductive branch of the Krebs cycle to support the production of oxaloacetate and malate through the activity of phosphoenolpyruvate carboxykinase and pyruvate carboxylase. Both branches terminate with the synthesis of malate, which is secreted. This unprecedented split of the Krebs cycle and malate secretion in a bacterial pathogen facilitates the continuous flow of carbon through the core of carbon metabolism, overcoming the metabolic stalling triggered by iron starvation.

During infection pathogenic bacteria are subject to nutritional immunity, a process in which the host alters metal availability to intoxicate or starve the invading pathogens (Murdoch & Skaar 2022). Metals are essential micronutrients that play structural, signaling or catalytic roles in most of cellular processes. Many enzymes of central metabolism depend on metals for their activity, however the effects of nutritional immunity on bacterial central carbon metabolism (CCM) have not been extensively investigated (Serafini 2021).

Over the past decade, mounting evidence has indicated a clear correlation between central metabolism and antibiotic resistance. It has been demonstrated that clinically relevant mutations in genes encoding core metabolic enzymes are associated to antibiotic resistance (Lopatkin et al. 2021)

and tolerance (Hicks et al. 2018). Furthermore, secondary or “collateral” effects of antibiotic action involve alterations to CCM (Wang et al. 2019; Kawai et al. 2019) and specific metabolic states affect their efficacy (Allison et al. 2011; Lim et al. 2021; Lopatkin et al. 2019; Schrader et al. 2021).

Mycobacterium tuberculosis (*Mtb*), the causative agent of tuberculosis (TB), has been recently included in the Bacterial Priority Pathogen List of the World Health Organization (WHO 2024) due to its intrinsic resistance to antibiotics and the increased spreading of multi-drug-resistant strains. Since the 1960s, only three new drugs have been approved for the treatment of TB (Murray et al. 2015; Zheng & Av-Gay 2016; Dartois & Dick 2024), and resistance to these new antibiotics is increasing. It is therefore critical that new medicines are developed to treat this infection. For more efficient antibiotic discovery, we must gain a more comprehensive understanding of the physiology of *Mtb* to assist the development of new therapies.

Experimental evidence indicates that *Mtb* is exposed to iron starvation during infection (Kurthkoti et al. 2017; Wells et al. 2013; Fang et al. 2015; Madigan et al. 2015; Pisu et al. 2020). This study aims to examine the relationship between iron homeostasis and CCM, a complex and understudied aspect of *Mtb* metabolism. *Mtb* exposed to prolonged and severe iron starvation exhibits a reduction in growth rate until replication is arrested, yet, cells remain viable (Kurthkoti et al. 2017). Based on the publicly available transcriptomic and proteomic data of H37Rv *Mtb* strain grown under iron limitation (**Dataset S1** and Kurthkoti et al. 2017; Wong et al. 1999; Serafini et al. 2013), we have recently proposed a model that explains how this pathogen might adapt its core of CCM to limited iron availability (Serafini 2021). We proposed that *Mtb*: i) reduces the activity of the Krebs cycle due to the compromised activity of its iron-dependent enzymes, which consequently reduces the production of $FADH_2$, NADH and ATP; ii) activates an iron-independent pathway, the glyoxylate shunt, to maintain succinate and malate production; iii) secretes succinate to maintain an energized cell membrane, bypassing the reduced ATP synthase activity.

The aim of the present study is to test these predictions thereby clarifying the effect of iron starvation on *Mtb* metabolism. We monitored metabolite levels using liquid chromatography coupled to mass spectrometry and employed ^{13}C isotope tracing to identify the metabolic pathways active under iron starvation. These experiments were conducted under the same growth conditions used in the more comprehensive transcriptomic study (Kurthkoti et al. 2017), which, like the other published studies on iron limitation (Wong et al. 1999; Serafini et al. 2013), included two carbon sources in the growth medium, glucose and glycerol. To circumvent genomic background-dependent effects, the work was performed in two *Mtb* strains with different metabolic capacities, H37Rv and Erdman (Serafini et al. 2019; Marrero et al. 2010).

Results

Severe growth defects accompany iron limitation

As demonstrated previously (Kurthkoti et al. 2017), *Mtb* exposed to severe iron starvation enters a non-replicative state that can persist for months. This severe iron starvation was achieved by subculturing bacteria in the absence of a source of Fe^{3+}, followed by the addition of the Fe^{3+} chelator deferoxamine (DFO), to trap any residual iron. Equivalent conditions were used in our laboratory to reproduce the growth arrest phenotype in Erdman and H37Rv (**Figure 1A-D)**. As expected, the absence of a Fe^{3+} source (0 μM $FeCl_3$) resulted in a growth defect, while the addition of DFO (0 μM $FeCl_3$ + DFO) led to growth arrest (**Figure 1A and B**). In the latter, Erdman exhibited an apparent decline in viability over several weeks (**Figure 1D**) compared to H37Rv (**Figure 1C**). This decline could be attributed to a more pronounced clumping of the cells in Erdman cultures (data not shown), that resulted in a reduction in the number of colony-forming units (CFUs), or to the cells entering an unculturable state (Kurthkoti et al. 2017).

Previous studies have shown that replication-arrest-inducing stress conditions such as hypoxia and nutrient starvation (Eoh & Rhee 2013; Rao et al. 2008; Gengenbacher et al. 2010) reduce ATP production and alter the NAD^+/NADH ratio. Transcriptomics data shows that upon Fe^{3+} depletion, *Mtb* down-regulates the operon encoding ATP synthase and the type I NADH dehydrogenase (**Dataset S1** and Kurthkoti et al. 2017; Serafini et al. 2013). We examined the levels of ATP and the NAD^+/NADH ratio. Surprisingly, ATP levels (**Figure 1G and H**) and the NAD^+/NADH ratio (**Figure 1I**) did not decrease upon Fe^{3+} depletion. Instead, an increase in ATP levels was observed in Erdman (**Figure 1H**). These results suggest that Fe^{3+} starvation causes a metabolic and physiological stress that is distinct from that observed in hypoxia and nutrient starvation (Rao et al. 2008; Gengenbacher et al. 2010; Eoh & Rhee 2013).

Slowdown of the Krebs cycle activity

Most genes encoding enzymes involved in the Krebs cycle exhibit a reduction in their expression levels over a two-week period in Fe^{3+}-starved H37Rv (**Dataset 1** and Kurthkoti et al. 2017). This finding indicates that the activity of this pathway may be reduced in such a condition. The levels of Krebs cycle intermediates were examined following an eight-day exposure to replete Fe^{3+} (50 μM $FeCl_3$, termed HI henceforth) compared to limiting Fe^{3+} (0 μM $FeCl_3$ and 0 μM $FeCl_3$+DFO, termed LI and DFO, respectively, henceforth). As the metabolomics analysis demonstrated highly comparable outcomes in the LI and DFO conditions, the subsequent sections will focus on the comparison between HI and DFO. Please refer to supplementary data (***Supplement file* section I**) for a detailed analysis in the LI condition.

In H37Rv, a consistent increase, exceeding a 100-fold change (FC), in the intracellular levels of pyruvate and α-ketoglutarate was observed in DFO compared to HI (**Figure 2A**). The accumulation of these two metabolites is in line with the downregulation of the *aceE*, *dlaT* and *lpdC* genes (**Dataset S1** and Kurthkoti et al. 2017), which encode subunits of the pyruvate dehydrogenase (PDH) and the α-ketoglutarate dehydrogenase (KDH) complexes (Tian et al. 2005; Shi & Ehrt 2006; Maksymiuk et

al. 2015). This accumulation is consistent with the existence of two stalling points at which the activity of the Krebs cycle is impeded, one before the cycle (PDH) and one at the KDH level. It is likely that the blockage at the level of pyruvate results in a slowdown the flux through glycolysis. The downregulation of glycolytic genes (**Dataset 1** and Kurthkoti et al. 2017) lends support to this hypothesis. A smaller increase in the levels of (iso)citrate was observed, with a 2- to 4-FC in two independent experiments (**Figure 2A**). This increase may be attributed to two potential mechanisms: i) citrate accumulation resulting from the reduced activity of the iron-dependent aconitase (Acn), which is also known to be down-regulated (Kurthkoti et al. 2017; Wong et al. 1999; Serafini et al. 2013); ii) isocitrate accumulation due to blockage of the Krebs cycle resulting in α-ketoglutarate accumulation. The succinate pool exhibited a statistically significant decrease in DFO, with intensity varying from 0.3- to 0.8-FC in two independent experiments (**Figure 2A**). No relevant alterations were observed in the levels of fumarate and malate. These results seem to contrast with the observation that genes encoding enzymes involved in the synthesis of fumarate and malate (fumarate reductase/Frd, fumarase/Fum and succinate dehydrogenase/Sdh) are iron-dependent and downregulated (**Dataset S1** and Kurthkoti et al. 2017) and therefore their activity should be lower under Fe^{3+} starvation. Surprisingly, the genes encoding the α-ketoglutarate ferredoxin-oxidoreductase KorAB complex (Baughn et al. 2009) are induced (Kurthkoti et al. 2017) suggesting that despite its iron-dependent nature, its activity is necessary to produce succinyl-CoA and then succinate from α-ketoglutarate.
As observed in H37Rv, in the Erdman strain (**Figure 2 – figure supplement 1A**) there is a substantial intracellular accumulation of pyruvate and α-ketoglutarate (>10 FC) and a more modest accumulation of (iso)citrate (1.2-2.8 FC, in four independent experiments) in DFO. No major changes were observed in the levels of malate, fumarate and succinate.
In conclusion, when experiencing Fe^{3+} starvation, *Mtb* slows down the activity of the Krebs cycle, and pyruvate conversion to acetyl-CoA and α-ketoglutarate conversion into succinyl-CoA may represent two distinct checkpoints in this process.

Substantial secretion of metabolic intermediates

The secretion of succinate has been linked to the maintenance of membrane potential in hypoxic growth-arrested *Mtb* (Eoh & Khee 2013). It has been demonstrated that in such condition the extracellular succinate levels increase and that the inhibition of its secretion (by supplementing the medium with succinate) causes alteration of the proton motive force and cell death (Eoh & Khee 2013). We hypothesized that succinate could have a similar role in DFO-treated cells (Serafini 2021). Levels of extracellular succinate were therefore monitored over a week period (1, 3 and 8 days). Unexpectedly, no change in succinate levels was observed in DFO, rather, a significant increase was noted in HI (**Figure 2B and Figure 2–figure supplement 1B**). Furthermore, the succinate levels were lower in DFO compared to the HI condition. Since *Mtb* cells remain viable in DFO (**Figure 1C and D**),

it can be concluded that the secretion of succinate is not a crucial factor in maintaining cell survival and membrane potential in such condition. This conclusion was confirmed by the observation that DFO-treated cells exposed to 2 mM succinate in the order to inhibit its secretion (Eoh & Khee 2013), remained viable (**Figure 2C and Figure 2–figure supplement 1C**), in contrast to the results observed during hypoxia.

Surprisingly, higher levels of several metabolic intermediates were found in the culture filtrate of DFO compared to HI cultures, with minor discrepancies between the H37Rv (**Figure 2B)** and Erdman (**Figure 2–figure supplement 1B**) strains. Fumarate, α-ketoglutarate, (iso)citrate, malate and pyruvate are secreted in substantial quantities and their levels increase over time, with the exception of fumarate. The levels of pyruvate and α-ketoglutarate increase by more than 10-fold, while those of (iso)citrate rise by 2- to 10-fold under Fe^{3+} starvation. The high levels of extracellular pyruvate, α-ketoglutarate and (iso)citrate are consistent with the elevated intracellular levels. It is noteworthy that malate levels exhibit a substantial increase, approximately 10-fold, in DFO compared to HI conditions that in H37Rv occurs after one day exposure to DFO conditions (**Figure 2B**) and at a later stage in the Erdman strain (**Figure 2-figure supplement 1B**). As the intracellular malate pool is constant under HI and DFO conditions, this increase in malate secretion suggests that this metabolite may be utilized for the maintenance of membrane potential. The viability of DFO-treated cells in the presence of malate was evaluated (**Figure 2–figure supplements 1C and 2A**) but no effect was observed on survival. The substantial secretion of several metabolites prompted the hypothesis that they may collectively contribute to the maintenance of the membrane potential. The experiment was then repeated adding pyruvate, α-ketoglutarate, succinate, malate and fumarate individually (**Figure 2–figure supplements 1C and 2A**) and in combination, yet again we saw no loss of viability. These results suggest that the secretion of these metabolites under Fe^{3+} starvation is unrelated to the maintenance of the membrane potential.

Partitioning of carbon flux into oxidative and reductive branches of Krebs cycle

The transcriptomic data from Fe^{3+}-starved H37Rv (Kurthkoti et al. 2017; Serafini et al. 2013), shows upregulation of isocitrate lyase 1 (*icl1/Rv04671*) (Honer Zu Bentrup et al. 1999) and phosphoenolpyruvate carboxykinase A (*pckA*/*Rv0211*) (Marrero et al. 2010; Machova et al. 2015) genes (**Dataset S1**). To verify the effective operation of these metabolic routes, cells were fed with $^{13}C_3$-glycerol and the isotopic labeling profiles of multiple metabolites reporting on CCM were analyzed (**Figures 3 and 4**).

Malate only partially derives from succinate oxidation

DFO-treated H37Rv shows a 50% reduction in labeled succinate compared to HI condition (**Figure 3**). This decrease is not observed in isocitrate and α-ketoglutarate, precursors of succinate. These

discrepancies suggest that a slower rate conversion of α-ketoglutarate into succinyl-CoA and subsequently into succinate, and of isocitrate to succinate may occur in DFO. The down-regulation of KDH complex genes (**Dataset S1** and Kurthkoti et al. 2017) supports the hypothesis related to α-ketoglutarate, however the up-regulation of *icl1* and *korAB* (see above) contradicts both hypotheses. The percentage of labeling observed in the malate pool (**Figure 3**) remains constant between the DFO and HI conditions. Notably, the percentage of malate labeling is significantly higher than that of succinate in DFO, indicating that some of the malate may not originate from succinate via fumarate. Unfortunately, the fumarate levels (**Figure 3**) were insufficient to permit the detection of labeling for this metabolite and verify if it is similar to malate rather than succinate. However, the comparison of the isotopologue distributions of malate and succinate confirms that some of the malate is not a product of succinate oxidation (**Figure 3**). Indeed, whereas in HI conditions the malate and succinate labeled pools show similar levels of M+1 and M+2 isotopologues (omitted isotopologue word after 'M+*n*' henceforth) and lower levels of M+3, in DFO M+2 succinate is more abundant compared to the M+1 and M+3, and M+3 malate is the most abundant (70 - 90% of total labeling) over M+1 and M+2 (**Figure 3**).

The DFO-treated Erdman strain does not show a marked decrease in the total labeling of succinate pool (**Figure 4**), and the isotopologue distribution shows that M+1 and M+2 are present at similar levels in the DFO and HI conditions. Similarly to H37Rv, in Erdman strain the malate labeled pool size was similar in DFO and HI conditions, and contains more M+3 in DFO compared to HI (40 – 50% of total labeling), with a clear decrease in M+1 an M+2 (**Figure 4**). In the Erdman strain, higher levels of fumarate were detected. Surprisingly, the labeled fumarate pool contained only M+1 in all conditions (**Figure 4**), impeding a more precise tracking of its origin. This specific labeling profile of fumarate is likely linked to the specific medium used in the current work (**Supplement file section II**).

Altogether, these results strongly suggest that up to 50% of the malate pool is not derived from succinate oxidation under the DFO condition in *Mtb*.

Malate mainly derives from oxaloacetate reduction

The upregulation of *icl1* and *pckA* genes under Fe^{3+} condition (Kurthkoti et al. 2017; Serafini et al. 2013) suggests that malate may be produced via isocitrate lyase (ICL) and phosphoenolpyruvate carboxykinase (PCK) activities, despite the conflicting differences in the total labeling (**Figure 3**) between isocitrate and succinate (see above). The increase of these enzymatic activities was confirmed in the cell-free extracts (**Figure 5A and B**).

Figures 3 and 4–figure supplements 1 and 2 show 31 possible metabolic scenarios for the production of core of CCM intermediates when the glyoxylate cycle and/or the PCK anaplerotic route are active. These scenarios combine labeled and unlabeled pyruvate, phosphoenolpyruvate (PEP), acetyl-CoA and carbon dioxide molecules. Although they do not consider the re-circulation of metabolites in the global metabolic circuit, these series of reactions offer a useful perspective on

identifying operating pathways. We compared these theoretical possibilities with our labeling data (isotopologue distribution) on succinate, malate, and (iso)citrate (**Figures 3 and 4**). Oxaloacetate was not included in this analysis due to technical limitations (**Supplement filesection III**). Of note, the isotopologue distribution of succinate is identical whether derived from isocitrate or from α-ketoglutarate.

Figure 3 and 4–figure supplement 1A-C show pyruvate dehydrogenase (PDH) and ICL activities. M+2 (iso)citrate, malate and succinate are the only isotopologues produced. This matches the experimental results for isocitrate and succinate, for which M+2 is one of the most abundant isotopologues (**Figure 3 and 4**). Of note, the medium used in these experiments contains asparagine, which represents an exogenous unlabeled source of oxaloacetate (**Supplement file section III**). This indicates that the **Figure 3 and 4–figure supplement 1A-C** scenarios are favored and explains the dominant abundance of M+2 (iso)citrate and succinate, compared to other isotopologues. However, these combinations do not produce the most abundant malate isotopologue, M+3, detected in our measurements.

Figure 3 and 4–figure supplement 1D-S show PCK and ICL activities. In these scenarios the M+3 malate isotopologue is present and derives from the glyoxylate shunt. However, there is no congruence between these theoretical scenarios and our labeling results (more details in **Supplement file Section IV**). This raises doubts about an active role of the glyoxylate shunt in the synthesis of malate.

Figure 3 and 4–figure supplement 2A-H illustrate alternative metabolic scenarios without the involvement of the glyoxylate shunt that include PCK activity and the oxidative branch of the Krebs cycle stopping at malate. Among these scenarios, the most represented isotopologues are M+3 for (iso)citrate (**Figure 3 and 4–figure supplement 2B and G**), M+2 for malate and for succinate (**Figure 3 and 4–figure supplement 2B, C, F and G**). These scenarios offer a rationale for the observed increase in M+3 (iso)citrate in our experiments in DFO (**Figure 3 and 4**), and imply that M+2 malate and succinate may originate from the oxidative branch of the Krebs cycle, fed via oxaloacetate produced by PCK (**Figure 3 and 4–figure supplement 2B, C, F and G**). These alternative scenarios align with those showed in **Figure 3 and 4–figure supplement 1A-C** for the synthesis of M+2 malate and succinate, excluding the glyoxylate shunt activity, but do not reveal the origin of M+3 malate.

We then hypothesized that PEP-derived oxaloacetate could proceed to the reductive branch of Krebs cycle (**Figure 3 and 4–figure supplement 2I-L**). The malate isotopologues produced in the **Figure 3 and 4–figure supplement 2I, K and L** scenarios are all detected in our experiments. The dominance of M+3 over M+1 (**Figure 3 and 4**) indicates that the scenario illustrated in **Figure 3 and 4–figure supplement 2I** is the most likely. The minor abundance of M+4 malate (**Figure 3 and 4)** is compatible with the unlikely possibility that an enzyme meets both substrates labeled (**Figure 3 and 4–figure supplement 2K**). A similar consideration is valid for the generation of M+4/M+5/M+6 (iso)citrate and M+4 succinate (**Figure 3 and 4–figure supplement 2A, E and F, Figures 3** and **4**). This new

analysis, which omits the glyoxylate shunt, is consistent with our experimental results and indicates that M+2 and M+4 malate derive from the oxidative branch of Krebs cycle, while M+1 and M+3 malate from the reductive branch. Further, these results indicate that, *pckA* has an important role in the CCM under Fe^{3+} starvation. Surprisingly, an Erdman-derived *pckA* mutant, which does not show loss of viability and reducing power under exposure to Fe^{3+} starvation (**Figure 1F and I**), does not show a significant decrease in M+3 malate and M+3 (iso)citrate in DFO (**Figure 5C and D**). In fact, there is no consistent between experiments (0-50% of decrease). Oxaloacetate can be produced directly from pyruvate by a pyruvate carboxylase (PCA) (Basu et al. 2018; Mukhopadhyay & Purwantini 2000), generating the same scenarios depicted in **Figure 3 and 4–figure supplement 1** and **2**, or malate can be directly produced from pyruvate by malic enzyme (MEZ) (**Figure 3 and 4–figure supplement 2M-P**). Measurement of the activity of these two enzymes in cell free extracts revealed the presence of PCA activity in the DFO condition (**Figure 5E**), but not of MEZ activity (data not shown). The absence of *pckA* does not result in an increase of PCA activity (**Figure 5F**), suggesting that the two activities work in parallel, but serve distinct and non-redundant functions. These results strongly suggest that *Mtb* utilizes anaplerotic reactions mediated by PCK and PCA to supply Krebs cycle intermediates under Fe^{3+} starvation (**Figure 3 and 4–figure supplement 2I**).

The glyoxylate shunt does not supply malate

To provide independent, genetic evidence supporting or ruling out the role of the glyoxylate shunt under Fe^{3+} starved conditions in H37Rv, the levels of succinate, malate and isocitrate were analyzed in an isocitrate lyase-deleted strain. H37Rv has two ICL enzymes, encoded by the *icl*1 and *aceAab* genes, however the second enzyme has a slower activity (Honer Zu Bentrup et al. 1999) and studies show that the inactivation of just *icl1* is relevant to alter *Mtb* physiology (Serafini et al. 2019; Gengenbacher et al. 2010). We used an H37Rv-Δ*icl1* and its complemented strain (Serafini et al. 2019), which is not essential for survival in DFO condition (**Figure 1E**). As the Δ*icl1* strain is not derived from the same H37Rv strain used in this study, metabolite abundance and isotopologue distribution in HI, LI and DFO conditions were verified and confirmed in the complemented strain (Δ*icl1::icl1*). Except for the lack of increase in intra- and extracellular (iso)citrate levels, all other trends were matched (**Figure 2 and 3–figure supplement 1**). If the glyoxylate shunt is a key supplier of malate and succinate, the absence of a functional ICL should result in a reduction in their abundance or labeling, an increase in isocitrate levels and a decrease in the M+2 in succinate. To our surprise, there are no discernible differences between the Δ*icl1* and the complemented strains, in the intracellular levels of these metabolites (**Figure 2 and 3–figure supplement 2A**) and in the isotopologue distribution of succinate and malate (**Figure 2 and 3–figure supplement 2B and C**) in DFO condition. We reasoned that in Δ*icl1* metabolite secretion could be diminished to maintain the intracellular abundance of malate and succinate or increased in the case of isocitrate. Again, there are no significant differences in the extracellular levels of these metabolites between the Δ*icl1* and the

complemented strains (**Figure 2 and 3–figure supplement 2E**). The results demonstrate that, despite the increase of ICL activity (**Fig. 5B**), the glyoxylate shunt is not playing an important role under Fe^{3+} starvation.

Next, we verified the operation of glyoxylate shunt in the Erdman strain by analyzing the levels and labeling profiles of intracellular metabolites in DFO-treated cells exposed to a potent inhibitor of mycobacterial ICL activity, 3-nitropropionate (3NP) (Honer Zu Bentrup et al. 1999; Moynihan & Murkin 2014), which does not affect survival under such condition (**Figure 2-figure supplement 2B**). The presence of 3NP did not increase the abundance of (iso)citrate, but rather that of α-ketoglutarate, and no relevant changes were detected in malate and succinate levels (**Figure 5G**). The isotopologue distribution analysis revealed no change in the abundance of the M+2 succinate in the DFO condition, but rather a diminution of the M+2 malate (**Figure 5H**). 3NP is also an inhibitor of Sdh (Alston et al. 1977), and the observed result appears to report on that, instead of on inhibition of ICL. These results also support the hypothesis that the glyoxylate shunt is not significantly active under Fe^{3+} depletion in *Mtb*.

GABA shunt generates succinate under iron starvation

The lack of evidence for an operational glyoxylate shunt under Fe^{3+} starvation led us to conclude that succinate must derive from α-ketoglutarate oxidation. The upregulation of the *korAB* genes (Kurthkoti et al. 2017) suggests that KorAB actively participates in succinyl-CoA synthesis. However, its iron-dependent nature together with the downregulation of succinyl-CoA synthetase genes (*sucCD*) suggests that an additional pathway, likely iron-independent, might be active under Fe^{3+} starvation conditions to maintain the succinate pool. This pathway is likely to be the γ-aminobutyric acid (GABA) shunt, an active route of CCM in Mtb (Serafini et al. 2019), which converts α-ketoglutarate into succinate bypassing succinyl-CoA synthesis (**Figure 6A**). Genes encoding GABA shunt enzymes are not differentially expressed under Fe^{3+} starvation conditions (**Dataset S1** and Kurthkoti et al. 2017; Serafini et al 2013).

In H37Rv, the levels and labeling of glutamate do not change to a major extent under HI and DFO conditions (**Figure 6B**). In contrast, we see a significant decrease in the GABA pool size in DFO (0.001 - 0.428 FC in four independent experiments), with a concomitant decrease in total labeling (reduction >50%) (**Figure 6C**). Changes in GABA abundance resemble that of succinate (**Figure 6D),** with a greater magnitude. This suggests that GABA might be used to produce succinate. We wondered if this reduction of the GABA pool could be due to its secretion, however we were not able to detect extracellular GABA (data not shown). The isotopologue distribution of the GABA and succinate pools (**Figure 6C and D**) are comparable to those of α-ketoglutarate (**Figure 3F**) with a notable reduction in the M+1 compared to the M+2.

Similar results were obtained in the Erdman strain (**Figure 6E-G**). The isotopologue distribution of succinate resembles that of GABA and glutamate, yet, it differs from that of α-ketoglutarate (**Figures 6E and 4F**). In particular, in succinate, GABA, and glutamate the levels of M+1 and M+2 are similar in DFO (**Figure 6E**), whereas M+2 α-ketoglutarate consistently exceeds M+1 (**Figure 4F**). This different isotopologue distribution in α-ketoglutarate suggests that the GABA shunt is significantly sustained by other metabolic circuits beyond α-ketoglutarate in Erdman.

The absence of a differential expression of GABA shunt genes under Fe^{3+} starvation and the similarity between the labeling profiles of succinate and GABA support the hypothesis that the GABA shunt maintains the succinate pool under Fe^{3+} starvation conditions in *Mtb*.

Discussion

The results presented here are summarized in **Figure 7**. The consistent accumulation of pyruvate and α-ketoglutarate identifies two check points of carbon flux through the CCM. This suggests that the proteins DlaT and LpdC, which are shared by the pyruvate and the α-ketoglutarate dehydrogenase complexes (Tian et al. 2005; Shi &Ehrt 2006; Maksymiuk et al.2015), play a critical role in this accumulation. Pyruvate and α-ketoglutarate are two key metabolites that intersect the energy and carbon/nitrogen metabolism. Their accumulation indicates that Fe^{3+} starvation slows down the overall cell metabolism. Despite this, *Mtb* cells survive and maintain a correct energy and redox balance (**Figure 1**). It has been observed that under Fe^{3+} starvation *Mtb* downregulates the proton pumping enzymatic complexes Type I NADH dehydrogenase (*nuoABCDEFGHIJKLMN*) and cytochrome oxidase bc_1-aa_3 (*qcrCAB*/*ctaBCED*) genes, whereas it upregulates the non-proton pumping Type II NADH dehydrogenase (*ndh*) gene and the gene for assembly of the less efficient and non-proton pumping cytochrome oxidase *bd* (*cydABDC*) (Kurthkoti et al. 2017; Serafini et al 2013; Cruz-Ramoset al. 2004). These changes in the electron transport chain suggest alterations in electron flow, proton secretion and likely ATP synthesis. The downregulation of the ATP synthase operon (*atpBEFHAGDC*) under Fe^{3+} deprivation (Kurthkoti et al. 2017) supports these observations but contrasts with our experimental results showing no changes in energy and redox balance (**Figure 2G and H**). The iron independent nature of Ndh may explain the opposite expression trend between type I and II NADH dehydrogenases and the fact that we see no redox imbalance; whereas reason behind the opposite trend between the two cytochrome oxidases is not clear. The induction of the non-proton pumping NADH dehydrogenase correlates with the downregulation of the ATP synthase operon. Intriguingly, the differential expression of *atpBEFHAGDC, ndh,* and *nuoABCDEFGHIJKLMN* genes in Fe^{3+} starvation is comparable to that seen during the efficient *Mtb* growth in L-lactate as a sole carbon source (Serafini et al. 2019). This suggests that the differential expression of these genes may result in altered activity of the corresponding enzymatic complexes, but not beyond the physiological

requirements of *Mtb*. It is also possible that other unknown mechanisms are activated to maintain ATP synthesis under these conditions.

The downregulation of transcripts for many CCM enzymes in Fe^{3+} starvation (Kurthkoti et al. 2017; Serafini et al 2013) is presumably a consequence of the slowed carbon flux, and the induction (Kurthkoti et al. 2017; Serafini et al 2013) of a few of them (*korAB*, *pckA* and *icl1*) is likely a strategy to sustain slowed carbon flow. The induction of the iron-dependent KorAB route represents a mechanism to bypass or parallel the KDH complex and GABA shunt, in order to sustain succinate synthesis and dispose of the accumulated α-ketoglutarate. This strategy combines multiple routes to maintain succinate synthesis under Fe^{3+}-starved conditions. A combination of multiple routes is also deployed to sustain carbon flux from PEP/pyruvate to the Krebs cycle. The anaplerotic reaction of PCK converts PEP into oxaloacetate, and it is flanked by PCA, which converts pyruvate into oxaloacetate. These two activities, together with PDH, represent three routes to control the level of pyruvate and sustain the carbon flux. Detailed ^{13}C tracking through Krebs cycle intermediates revealed an unexpected split of carbon flux from PEP- and pyruvate-derived oxaloacetate to both the oxidative and reductive branches of the Krebs cycle. Oxaloacetate is partitioned between oxidation to citrate and reduction to malate, with the latter route being the most favorable (**Figures 3 and 4**, **Figure 3 and 4–figure supplements 1 and 2**). The two fluxes converge to produce malate, the extracellular level of which increases (**Figure 7**). The production of oxaloacetate via PCK and PCA under Fe^{3+} starvation occurs despite the presence of an exogenous source of oxaloacetate (the asparagine in the medium, **Supplement file section III**), and clearly demonstrates the importance of these anaplerotic reactions in Fe^{3+} starvation beyond oxaloacetate synthesis. This indicates that the anaplerotic reactions of PCK and PCA have another function. These activities likely control pyruvate levels but also may contribute to assimilating the excess of carbon dioxide stoichiometrically produced with α-ketoglutarate by isocitrate dehydrogenase (Icd, **Figure 7**). The *pckA* gene is also induced in Fe^{3+} starvation when glutamate and ammonium, but not asparagine, are present as nitrogen sources in the medium (Serafini et al. 2013). This induction suggests that PCK and likely PCA are the main producers of oxaloacetate.

The significant quantities of extracellular malate under Fe^{3+} starvation, despite its intracellular levels being similar to those in Fe^{3+} replete condition, suggests that secretion of this metabolite has a functional role. Also, the reduced secretion of succinate under Fe^{3+} starvation seems to indicate that succinate (**Figure 2 and Figure 2-figure supplement 1**) is required to produce malate. The secretion of malate may promote carbon flux through the anaplerotic node to relieve the accumulation of metabolic intermediates from the oxidative branch of the Krebs cycle. NADH re-oxidation mediated by malate dehydrogenase might contribute to maintaining the redox state of cells, together with Ndh. The upregulation of *icl1* (Kurthkoti et al. 2017; Serafini et al. 2013) and the resulting increase of ICL activity under Fe^{3+} starvation appear to be dispensable for the synthesis of malate and succinate (**Figure 2 and 3-figure supplement 2 and Figure 5**), which is surprising considering that the

glyoxylate shunt has been demonstrated to be important for the survival of *Mtb* under various growth arrest-causing conditions (Eoh & Rhee 2013; Genegenbacher et al. 2010; Nandakumar et al. 2014). On the other hand, the key function of the glyoxylate shunt is to bypass the two Krebs cycle decarboxylation reactions, and thereby "save up" carbon. Under our experimental conditions, carbon is replete, and therefore the glyoxylate shunt is not needed. Alternatively, ICL-derived glyoxylate may be transformed into glycine by a glycine dehydrogenase as previously demonstrated under hypoxia (Giffin et al. 2012). This activity is performed by alanine dehydrogenase (ALD), which is upregulated under Fe^{3+} depletion (Kurthkoti et al. 2017). It would be interesting to experimentally verify the presence, or rather an increase, of glycine dehydrogenase activity in *Mtb* starved for Fe^{3+}.

The induction of ICL under Fe^{3+} starvation is not unique to mycobacteria. An increase of its activity has been observed in *Pseudomonas aeruginosa* under Fe^{3+} starvation (Ha et al. 2018) and in *Pseudomonas fluorescens* under Al^{3+} stress, which mimics iron deficiency (Middaugh et al. 2005). In *P. aeruginosa*, the absence of ICL activity causes an increase in succinate dehydrogenase activity suggesting its involvement in succinate synthesis (Ha et al. 2018). It is noteworthy that *P. aeruginosa icl* mutant accumulates intracellular iron, suggesting a role beyond CCM. Unfortunately, metabolomics studies have not been performed in this mutant. Interestingly, it has been demonstrated that *P. fluorescens* exposed to Al^{3+} stress induces an acylating glyoxylate dehydrogenase (AGODH) that transforms glyoxylate to oxalyl-CoA and then oxalate, a molecule necessary to seize Al^{3+} ions (Singh et al. 2009). Coenzyme A is recycled to produce succinyl-CoA and then succinate, releasing one ATP (Singh et al. 2009). The finding that glyoxylate is used in a metabolic pathway functional for Al^{3+} stress, rather than for malate synthesis, supports the hypothesis that *Mtb* may use ICL for an alternative metabolic function under Fe^{3+} starvation.

In conclusion, this study has elucidated a novel metabolic strategy employed by *Mtb* to adapt to the diminished efficiency of iron-dependent enzymes. Partition of metabolic flux between reductive and oxidative branches of Krebs cycle producing and secreting malate is unprecedented metabolic adaptation for a bacterial pathogen.

Materials and Methods

Bacterial strains and growth conditions

In this study H37Rv and Erdman *M. tuberculosis* strains were used. *ΔpckA* and *ΔpckA*::*pckA* (Marrero et al. 2010) (Erdman genomic background) were kindly provided by Professor Sabine Ehrt (Weill Cornell Medicine). The *Δ*icl1 (Lee et al. 2013) strain was kindly provided by Professor Brian VanderVen (Cornell University). The *Δicl1*::*icl1* strain was previously generated (Serafini et al. 2019). For the metabolomic experiments in the Erdman genomic background, the strain *ΔpckA*::*pckA* was used (named Erdman strain in the text and figures and named *ΔpckA*::*pckA* in the comparison with *ΔpckA*).

Bacteria were routinely cultivated at 37 °C in 7H9/7H10 medium supplemented with ADC (0.5% bovine serum albumin 0.2% glucose, 0.085% NaCl, 0.003% catalase), 0.05% Tween80 and 0.2% glycerol. Mutant and complemented strains were grown in the presence of selective antibiotics in the 7H9/7H10 pre-cultures. Antibiotics were added at the following concentrations: 20 µg/ml kanamycin (Km); 10 µg/ml gentamicin (Gm); 100 µg/ml hygromycin (Hyg).

For all the experiments bacteria were cultivated in minimal medium (MM; 0.5% w/v KH_2PO_4; 0.5 % w/v asparagine; 0.2% glycerol; 0.05% tyloxapol; 0.5% bovine serum albumin 0.2% D-glucose, 0.085% NaCl, pH 6.8) treated with Chelex100 resin (Sigma) at RT for 24 h, replacing Chelex 100 resin after 12 h. The resin was removed by filtration and the medium was supplemented with 40 mg/L $MgSO_4$; 0.1 mg/L $MnSO_4$ and $ZnSO_4$ 0.5 mg/L. For the labeling experiments, 0.2% glycerol was replaced with a mixture of 0.1% $^{12}C_3$-glycerol and 0.1% $^{13}C_3$-glycerol. The choice of glycerol as the labeled carbon source was based on the superior ability of H37Rv to metabolize this substrate compared to glucose (Serafini et al. 2019).

A source of Fe^{3+} (50 µM of $FeCl_3$) was added only in the control condition (High Iron, HI). All the tests of this study were performed in bacterial cells sub-cultured three times (4-7 days of growth) in MM supplemented with (HI) or without (0 µM of $FeCl_3$, Low Iron, LI) a Fe^{3+} source. To get growth arrest, twice sub-cultured bacterial cells grown without a source of Fe^{3+} were treated with the siderophore deferoxamine mesylate salt (DFO) at a final concentration of 50 ng/mL[15]. For each experiment parallel HI and LI cultures were also treated. For metabolomics samples, MM was prepared omitting tyloxapol, which interferes with LC-MS analysis (MM No Tyloxapol, MMNT).

All the growth experiments in liquid cultures were performed in standing in T75 (25 mL of culture)/T25 (10 mL of culture) flasks laid down on the incubator floor to optimize the oxygenation, with daily gentle manual shaking.

The input of cells was approximately 1×10^7 cells/mL for CFU/growth assay and 2×10^7 cells/mL for all the other analysis (metabolite content, ATP and NADH assays).

Cell viability was assessed by counting Colony Forming Unit (CFU) /mL or by spot density on 7H10/ADC plates. CFU/mL: bacterial culture was serially diluted 10-fold and 50 µL of each dilution was plated in duplicate. Spot's density: bacterial culture was diluted to 10^7 cells/mL (OD_{600} ~0.1) and subjected to four 1:10 serial dilutions (10^6 to 10^2 cells/mL); 5 µL of each dilution was spotted on the plate.

Protein extraction and enzymatic activity

Approximately 10-15 OD_{600} of a bacterial culture were harvested and washed three times with cold PBS 1X and then the pellet resuspended in 600 µL of extraction buffer (DPBS 1X and Complete EDTA-free protease inhibitor cocktail). The cells were disrupted by using acid-washed glass beads (2:1 = buffer volume: beads volume) and a refrigerated beat-beater (6.0 set, 35'' pulses/1' pause twice). After centrifugation at 13,000 rpm for 15 min at 4 °C, the supernatant was filtered with a PVDF

filter tube before removal from the BLS3 laboratory. Within 6 hrs after extraction, enzymatic activity assays were performed using 10 µl of extract in a 96-well polystyrene microplate, with a final reaction volume of 200 µl. Protein content was determined using the Bradford reagent.

The anaplerotic activity of phosphoenolpyruvate carboxylase was determined as previously described (Machova et al. 2015) coupling the phosphoenolpyruvate carboxylation to oxaloacetate and malate synthesis by using malate dehydrogenase (pig heart, Sigma). The reaction was performed at 37 °C in a buffer containing HEPES/NaOH pH 7.2 100 mM, $KHCO_3$ 100 mM, DTT 37 mM, sodium phosphoenolpyruvate 2 mM, GDP 1 mM, $MgCl_2$ 2 mM, $MnCl_2$ 0.1 mM, malate dehydrogenase 3.5 U/ml, NADH 0.25 mM. The reaction was initiated by adding the $MgCl_2$ and $MnCl_2$. The decrease of absorbance at 340 nm was measured to monitor NADH oxidation.

Pyruvate carboxylase activity was determined as previously described (Mukhopadhyay & Purwantini 2000) coupling the phosphoenolpyruvate carboxylation to oxaloacetate and malate synthesis by using malate dehydrogenase. The reaction was performed at 37°C in a buffer containing Tris/HCl pH 8.0 50 mM, $KHCO_3$ 20 mM, $MgCl_2$ 8 mM, di-sodium ATP 8 mM, acetyl-CoA 50 µM, di-sodium NADH 0.2 mM, malate dehydrogenase 3.5 U/ml and sodium pyruvate 20 mM. The reaction was initiated by adding pyruvate. The decrease of absorbance at 340 nm was measured to monitor NADH oxidation.

Malic enzyme activity was determined as previously described (Basu et al. 2018). The reaction was performed at 30 °C in a buffer containing Tris/HCl pH 6.0 100 mM, $KHCO_3$ 200 mM, $MnCl_2$ 0.5 mM, NAD(P)H 0.6 mM, and sodium pyruvate 50 mM. The reaction was initiated by adding pyruvate. The decrease of absorbance at 340 nm was measured to monitor NAD(P)H oxidation.

Isocitrate lyase activity was determined as previously described (Munoz-Elias et al. 2006). The reaction was performed at 25 °C in a buffer containing MOPS-HCl pH 6.8 50 mM, $MgCl_2$ 5 mM, NADH 0.1 mM, 7U L-lactate dehydrogenase (Rabbit). The reaction was pre-incubated 5 minutes at 25 °C and then 1 mM of DL-*threo*-isocitrate was added. The decrease of absorbance at 340 nm was measured to monitor NADH oxidation.

Metabolite extraction and LC-MS analysis

Cells were sub-cultured twice in MM supplemented with 50 or 0 µM of $FeCl_3$, then washed once to remove tyloxapol and resuspended to a final absorbance of 0.2 in 10 mL of MMNT supplemented with 50, 0 µM of $FeCl_3$ and 0 µM of $FeCl_3$ +DFO. MMNT contained 0.2% of D-glucose, 0.1% of glycerol and 0.1% of (U)-^{13}C-labeled glycerol. Cultures were incubated standing at 37 °C. Intracellular polar metabolites were extracted after 8 days by mechanical rupture in an acetonitrile:methanol:water (2:2:1, v/v/v) solution as previously described (Serafini et al. 2019). Extracellular metabolites were extracted after 1, 3 and 8 days by diluting the culture-filtrate 1:5 using cold acetonitrile/methanol (1:1) supplemented with 0.1% formic acid; the samples were vigorously vortexed and stored at -20 °C for 2 hours; they were spun down for 10 minutes at 14,000 rpm and 4 °C, then filtered through 0.22 µm filter tubes.

2 µl of pellet extract and 10 µL of culture-filtrate extract were injected in a 1200 Liquid Chromatography system (Agilent) coupled to an Accurate Mass 6220 TOF (Agilent). Polar elution was performed as previously described using a gradient of two solvents, A (mQ water and 0.1% of formic acid) and B (acetonitrile and 0.1% of formic acid) (Serafini et al. 2019).
Intracellular metabolites were normalized by the residual peptide content detected using a BCA assay. Extracellular metabolites were normalized by total ion counts detected by Progenesis software. To plot the data, each normalized value was multiplied or divided for the same number, then the y axis plots report an arbitrary unit.
Due to technical limitations, the phosphorylated intermediates of glycolysis and oxaloacetate could not be analyzed.

ATP and NADH/NAD assays

The ATP assay was performed using the Promega BacTiter-Glo Microbial Cell Viability assay (G8232). Three technical replicates (three aliquots of cells) were performed for each experiment using approximately 10^7 cells/well (0.1 OD_{600}). ATP levels were assessed using an ATP standard curve (µM) and values normalized to OD_{600}.The NADH/NAD ratio was determined using the Promega NAD/NADH-Glo assay (G9071). Cells were collected, cooled on ice, and resuspended in a buffer containing PBS, NaOH and dodecyltrimethylammonium bromide according to the kit. The cells were then disrupted with a beat-beater (30'' 6.5 power at 4 °C) and the extracts were filtered through 0.22 µm filter tubes. The levels of NADH and NAD were then determined according to the kit instructions using NAD and NADH calibration curves. Two technical replicates were performed for each experiment using approximately 3×10^7 cells.

Statistical analysis

Data were expressed as average and standard deviations. Statistical correlations of data were checked for significance using the paired Student T test (p value <0.05).

Acknowledgments

Research funded by H2020 European Commission Program (MSCA-IF GA N. 101029081) and EU funding within the MUR PNRR Extended Partnership initiative on Emerging Infectious Diseases (project no. PE00000007, INF-ACT). We thank Dr Giuseppe Giordano from Pediatric Research Institute Foundation for access to the Progenesis software.

Author's contribution

A.S. conceptualized the study, performed experiments, analyzed and interpreted data, and wrote the manuscript. A.G. developed the protocol to extract metabolites from culture-filtrate samples, extracted

metabolites from the culture-filtrate samples and processed the metabolomics samples in the LC-MS instrument. D.S. performed the isocitrate lyase activity experiment. L.P.S.C. critically reviewed the manuscript. A.G., D.S and R.M. contributed to revise the final draft of the manuscript.

References

Murdoch CC, Skaar EP. 2022. Nutritional immunity: the battle for nutrient metals at the host-pathogen interface. *Nat Rev Microbiol* **20**: 657-670. https://dx.doi.org/10.1038/s41579-022-00745-6, PMID: 35641670.

Serafini A. 2021. Interplay between central carbon metabolism and metal homeostasis in mycobacteria and other human pathogens. *Microbiology (Reading)* **167** (6). https://dx.doi.org/10.1099/mic.0.001060, PMID: 34080971.

Lopatkin AJ, Bening SC, Manson AL, Stokes JM, Kohanski MA, Badran AH, Earl AM, Cheney NJ, Yang JH, and Collins JJ. 2021. Clinically relevant mutations in core metabolic genes confer antibiotic resistance. *Science* **371**(6531):eaba0862. doi: 10.1126/science.aba0862, PMID: 33602825

Hicks ND, Yang J, Zhang X, Zhao B, Grad HY, Liu L, Ou X, Chang Z, Xia H, Zhou Y, Wang S, Dong J, Sun L, Zhu Y, Zhao Y, Jin Q, Fortuna SM. 2018. Clinically prevalent mutations in Mycobacterium tuberculosis alter propionate metabolism and mediate multidrug tolerance. *Nat Microbiol* **3**(9):1032-1042. doi:10.1038/s41564-018-0218-3, PMID: 30082724

Wang Z, Soni V, Marriner G, Kaneko T, Boshoff HIM, Barry CE, Rhee KY. 2019. Mode-of-action profiling reveals glutamine synthetase as a collateral metabolic vulnerability of *M. tuberculosis* to bedaquiline. *Proc Natl Acad Sci U S A* **116**: 19646-19651. doi: 10.1073/pnas.1907946116, PMID: 31501323

Kawai Y, Mercier R, Mickiewicz K, Serafini A, Sório de Carvalho LP, Errington J. 2019. Crucial role for central carbon metabolism in the bacterial L-form switch and killing by β-lactam antibiotics. *Nat Microbiol* **4**: 1716-1726. doi: 10.1038/s41564-019-0497-3, PMID: 31285586

Allison KR, Brynildsen MP, Collins JJ. 2011. Metabolite-enabled eradication of bacterial persisters by aminoglycosides. *Nature* **473**(7346):216-20. doi:10.1038/nature10069 PMID: 21562562

Lim J, Lee JJ, Lee SK, Kim S, Eum SY, Eoh H. 2021. Phosphoenolpyruvate depletion mediates both growth arrest and drug tolerance of *Mycobacterium tuberculosis* in hypoxia. *Proc Natl Acad Sci U S A* **118** (35):e2105800118. doi: 10.1073/pnas.2105800118, PMID: 34426499

Lopatkin AJ, Stokes JM, Zheng EJ, Yang JH, Takahashi MK, You L, Collins JJ. 2019. Bacterial metabolic state more accurately predicts antibiotic lethality than growth rate. *Nat Microbiol* **4**: 2109-2117. doi: 10.1038/s41564-019-0536-0, PMID: 31451773

Schrader SM, Botella H, Jansen R, Ehrt S, Rhee K, Nathan C, Vaubourgeix J. 2021. Multiform antimicrobial resistance from a metabolic mutation. *Sci Adv* **7**(35):eabh2037**.** doi: 10.1126/sciadv.abh2037, PMID: 34452915

WHO Bacterial Priority Pathogens List 2024: Bacterial Pathogens of Public Health Importance, to Guide Research, Development, and Strategies to Prevent and Control Antimicrobial Resistance. World Health Organization, Geneva. Licence: CC BY-NC-SA 3.0 IGO.

Murray JF, Schraufnagel DE, Hopewell PC. 2015. Treatment of Tuberculosis. A Historical Perspective. *Ann Am Thorac Soc* **12**: 1749-1759. doi: 10.1513/AnnalsATS.201509-632PS, PMID: 26653188

Zheng X, Av-Gay Y. 2016. New Era of TB Drug Discovery and Its Impact on Disease Management. *Curr Treat Options Infect Dis* **8**: 299-310. doi: 10.1007/s40506-016-0098-0

Dartois V, and Dick T. 2024. Therapeutic developments for tuberculosis and nontuberculous mycobacterial lung disease. *Nat Rev Drug Discov* **23**: 381-403. doi: 10.1038/s41573-024-00897-5, PMID: 38418662

Kurthkoti K, Amin H, Marakalala MJ, Ghanny S, Subbian S, Sakatos A, Livny J, Fortune SM, Berney M, Rodriguez GM. 2017. The capacity of *Mycobacterium tuberculosis* to survive iron starvation might enable it to persist in iron-deprived microenvironments of human granulomas. *mBio* **8**(4):e01092-17. DOI: 10.1128/mBio.01092-17, PMID: 28811344

Wells RM, Jones CM, Xi Z, Speer A, Danilchanka O, Doornbos KS, Sun P, Wu F, Tian C, Nederweis M. 2013. Discovery of a siderophore export system essential for virulence of Mycobacterium tuberculosis. *PLoS Pathog*. **9**(1):e1003120. doi:10.1371/journal.ppat.1003120, PMID: 23431276

Fang Z, Sampson SL, Warren RM, Gey van Pittius NC, Newton-Foot M. 2015. Iron acquisition strategies in mycobacteria. Tuberculosis (Edinb). **95**(2):123-30. doi: 10.1016/j.tube.2015.01.004. 17. PMID: 25636179

Madigan CA, Martinot AJ, Wei JR, Madduri A, Cheng TY, Young DC, Layre E, Murry JP, Rubin EJ, Moody DB. 2015. Lipidomic analysis links mycobactin synthase K to iron uptake and virulence in M. tuberculosis. PLoS Pathog. **11**(3):e1004792. doi: 10.1371/journal.ppat.1004792. PMID: 25815898

Pisu D, Huang L, Grenier JK, Russell DG. 2020. Dual RNA-Seq of Mtb-Infected Macrophages In Vivo Reveals Ontologically Distinct Host-Pathogen Interactions. Cell Rep. **30**(2):335-350.e4. doi: 10.1016/j.celrep.2019.12.033. PMID: 31940480

Wong DK, Lee BY, Horwitz MA, Gibson BW. 1999. Identification of fur, aconitase, and other proteins expressed by *Mycobacterium tuberculosis* under conditions of low and high concentrations of iron by combined two-dimensional gel electrophoresis and mass spectrometry. *Infect Immun* **67**: 327-336. DOI: 10.1128/IAI.67.1.327-336.1999, PMID: 9864233

Serafini A, Pisu D, Palù G, Rodriguez GM, Manganelli R. 2013. The ESX-3 secretion system is necessary for iron and zinc homeostasis in *Mycobacterium tuberculosis*. *PLoS One* **8**: e78351. DOI: 10.1371/journal.pone.0078351, PMID: 24155985

Serafini A, Tan L, Horswell S, Howell S, Greenwood DJ, Hunt DM, Phan MD, Schembri M, Monteleone M, Montague CR, Britton W, Garza-Garcia A, Snijders AP, VanderVen B, Gutierrez MG, West NP,

de Carvalho LPS. 2019. *Mycobacterium tuberculosis* requires glyoxylate shunt and reverse methylcitrate cycle for lactate and pyruvate metabolism. *Mol Microbiol* **112**: 1284-1307. DOI: 10.1111/mmi.14362, PMID: 31389636

Marrero J, Rhee KY, Schnappinger D, Pethe K, Ehrt S. 2010. Gluconeogenic carbon flow of tricarboxylic acid cycle intermediates is critical for *Mycobacterium tuberculosis* to establish and maintain infection. *Proc Natl Acad Sci U S A* **107**: 9819-9824. DOI: 10.1073/pnas.1000715107, PMID: 20439709

Rao SP, Alonso S, Rand L, Dick T, Pethe K. 2008. The protonmotive force is required for maintaining ATP homeostasis and viability of hypoxic, nonreplicating *Mycobacterium tuberculosis*. *Proc Natl Acad Sci U S A* **105**: 11945-11950. DOI: 10.1073/pnas.0711697105, PMID: 18697942

Gengenbacher M, Rao SPS, Pethe K, Dick T. 2010. Nutrient-starved, non-replicating *Mycobacterium tuberculosis* requires respiration, ATP synthase and isocitrate lyase for maintenance of ATP homeostasis and viability. *Microbiology (Reading)* **156**: 81-87. DOI: 10.1099/mic.0.033084-0, PMID: 19797356

Eoh H, Rhee KY. 2013. Multifunctional essentiality of succinate metabolism in adaptation to hypoxia in *Mycobacterium tuberculosis*. *Proc Natl Acad Sci U S A* **110**: 6554-6559. DOI: 10.1073/pnas.1219375110, PMID: 23576728

Tian J, Bryk R, Shi S, Erdjument-Bromage H, Tempst P, Nathan C. 2005. *Mycobacterium tuberculosis* appears to lack alpha-ketoglutarate dehydrogenase and encodes pyruvate dehydrogenase in widely separated genes. *Mol Microbiol* **57**: 859-868. DOI: 10.1111/j.1365-2958.2005.04741.x, PMID: 16045627

Shi S, Ehrt S. 2006. Dihydrolipoamide acyltransferase is critical for *Mycobacterium tuberculosis* pathogenesis. *Infect Immun* **74**: 56-63. DOI: 10.1128/IAI.74.1.56-63.2006, PMID: 16368957

Maksymiuk C, Balakrishnan A, Bryk R, Rhee KY, Nathan CF. 2015. E1 of α-ketoglutarate dehydrogenase defends *Mycobacterium tuberculosis* against glutamate anaplerosis and nitroxidative stress. *Proc Natl Acad Sci U S A* **112**: E5834-5843. DOI: 10.1073/pnas.1510932112, PMID: 26430237

Baughn AD, Garforth SJ, Vilchèze C, Jacobs WR. 2009. An anaerobic-type alpha-ketoglutarate ferredoxin oxidoreductase completes the oxidative tricarboxylic acid cycle of *Mycobacterium tuberculosis*. *PLoS Pathog* **5**: e1000662. DOI: 10.1371/journal.ppat.1000662, PMID: 19936047

Höner Zu Bentrup K, Miczak A, Swenson DL, Russell DG. 1999. Characterization of activity and expression of isocitrate lyase in *Mycobacterium avium* and *Mycobacterium tuberculosis*. *J Bacteriol* **181**: 7161-7167. DOI: 10.1128/JB.181.23.7161-7167.1999, PMID: 10572116

Machová I, Snašel J, Zimmermann M, Laubitz D, Plocinski P, Oehlmann W, Singh M, Dostál J, Sauer U, Pichová I. 2015. *Mycobacterium tuberculosis* phosphoenolpyruvate carboxykinase is regulated by redox mechanisms and interaction with thioredoxin. *J Biol Chem* **289**: 13066-13078. DOI: 10.1074/jbc.M113.536748, PMID: 24659783

Basu P, Sandhu N, Bhatt A, Singh A, Balhana R, Gobe I, Crowhurst NA, Mendum TA, Gao L, Ward JL, Beale MH, McFadden J, Beste DJV. 2018. The anaplerotic node is essential for the intracellular survival of. *J Biol Chem* **293**: 5695-5704. DOI: 10.1074/jbc.RA118.001839, PMID: 29475946

Mukhopadhyay B, Purwantini E. 2000. Pyruvate carboxylase from *Mycobacterium smegmatis*: stabilization, rapid purification, molecular and biochemical characterization and regulation of the cellular level. *Biochim Biophys Acta* **1475**: 191-206. DOI: 10.1016/s0304-4165(00)00064-7, PMID: 10913817

Moynihan MM, Murkin AS. 2014. Cysteine is the general base that serves in catalysis by isocitrate lyase and in mechanism-based inhibition by 3-nitropropionate. *Biochemistry* **53**: 178-187. DOI: 10.1021/bi401432t, PMID: 24354272

Alston TA, Mela L, Bright HJ. 1977. 3-Nitropropionate, the toxic substance of Indigofera, is a suicide inactivator of succinate dehydrogenase. *Proc Natl Acad Sci U S A* **74**: 3767-3771. DOI: 10.1073/pnas.74.9.3767, PMID: 269430

Cruz-Ramos H, Cook GM, Wu G, Cleeter MW, Poole RK. 2004. Membrane topology and mutational analysis of *Escherichia coli* CydDC, an ABC-type cysteine exporter required for cytochrome assembly. *Microbiology* (Reading) 150: 3415-3427. DOI: 10.1099/mic.0.27191-0, PMID: 15470119

Nandakumar M, Nathan C, Rhee KY. 2014. Isocitrate lyase mediates broad antibiotic tolerance in *Mycobacterium tuberculosis*. *Nat Commun* **5**: 4306. DOI: 10.1038/ncomms5306, PMID: 24978671

Giffin MM, Modesti L, Raab RW, Wayne LG, Sohaskey CD. 2012. ald of *Mycobacterium tuberculosis* encodes both the alanine dehydrogenase and the putative glycine dehydrogenase. *J Bacteriol* **194**: 1045-1054. DOI: 10.1128/JB.05914-11, PMID: 22210765

Ha S, Shin B, Park W. 2018. Lack of glyoxylate shunt dysregulates iron homeostasis in *Pseudomonas aeruginosa*. *Microbiology (Reading)* **164**: 587-599. DOI: 10.1099/mic.0.000623, PMID: 29465342

Middaugh J, Hamel R, Jean-Baptiste G, Beriault R, Chenier D, Appanna VD. 2005. Aluminum triggers decreased aconitase activity via Fe-S cluster disruption and the overexpression of isocitrate dehydrogenase and isocitrate lyase: a metabolic network mediating cellular survival. *J Biol Chem* **280**: 3159-3165. DOI: 10.1074/jbc.M411979200, PMID: 15548528

Singh R, Lemire J, Mailloux RJ, Chénier D, Hamel R, Appanna VD. 2009. An ATP and oxalate generating variant tricarboxylic acid cycle counters aluminum toxicity in *Pseudomonas fluorescens*. *PLoS One* **4**: e7344. DOI: 10.1371/journal.pone.0007344, PMID: 19809498

Lee W, VanderVen BC, Fahey RJ, Russell DG. 2013. Intracellular *Mycobacterium tuberculosis* exploits host-derived fatty acids to limit metabolic stress. *Journal of Biological Chemistry*, 288, 6788–6800. DOI: 10.1074/jbc.M112.445056, PMID: 23306194

Munoz-Elias EJ, Upton AM, Cherian J, McKinney JD. 2006. Role of the methylcitrate cycle in *Mycobacterium tuberculosis* metabolism, intracellular growth, and virulence. *Molecular Microbiology*, 60, 1109–1122. doi: 10.1111/j.1365-2958.2006.05155.x, PMID: 16689789

Figures and legends

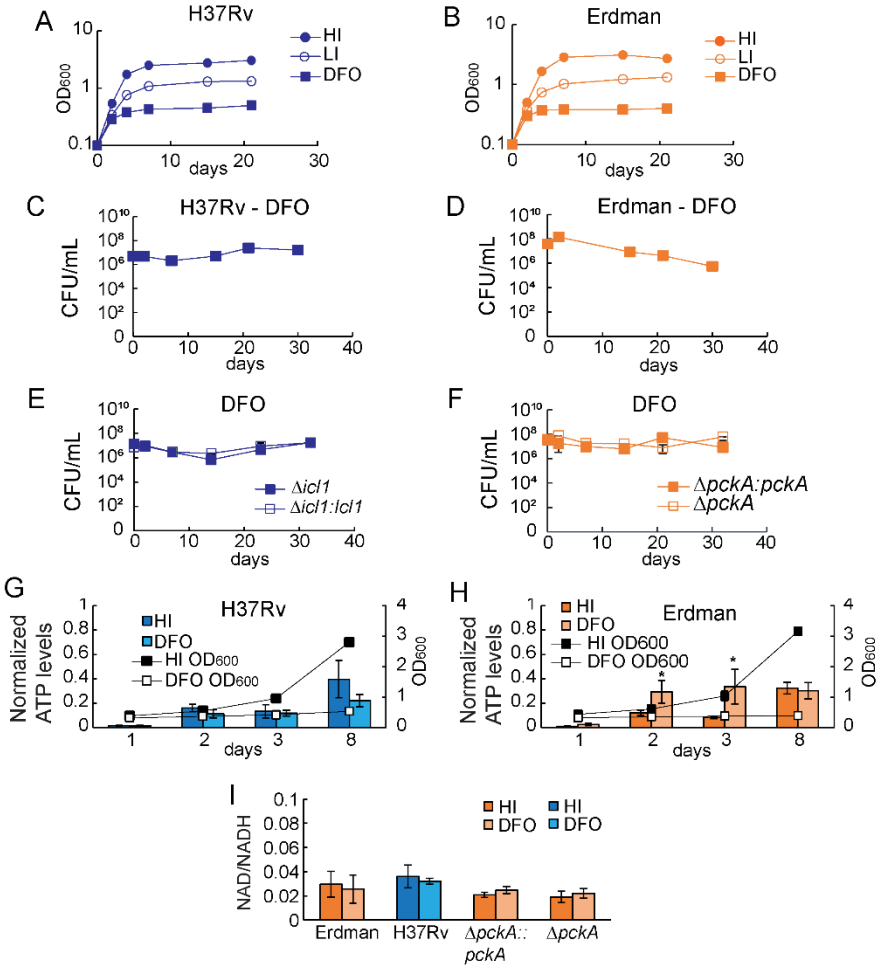

Figure 1. Survival to Fe^{3+} starvation in *Mtb* H37Rv and Erdman strains. Cells were exposed to 50 µM $FeCl_3$ (HI: High Iron), 0 µM $FeCl_3$ (LI: Low Iron,) or 0 µM $FeCl_3$+ DFO (DFO). Growth was monitored for 3 weeks by measuring OD_{600} (A, B), and survival was monitored for more than 4 weeks by CFU/mL (C, D, E, F). The charts show one experiment representative of 2-3 independent experiments. The CFU/mL charts show average and average deviation of two technical replicates of one independent experiment. G, H) ATP levels and growth (OD_{600}) after 1, 2, 3 and 8 days in DFO. ATP levels were normalized to the optical density. The data are the average and standard deviation of three independent experiments and three technical replicates each. I) NAD/NADH ratio detected after 3 days of exposure to DFO. The data are the average and standard deviation of two independent experiments and two technical replicates. The p-values were calculated against the HI condition.
* = p value < 0.05.

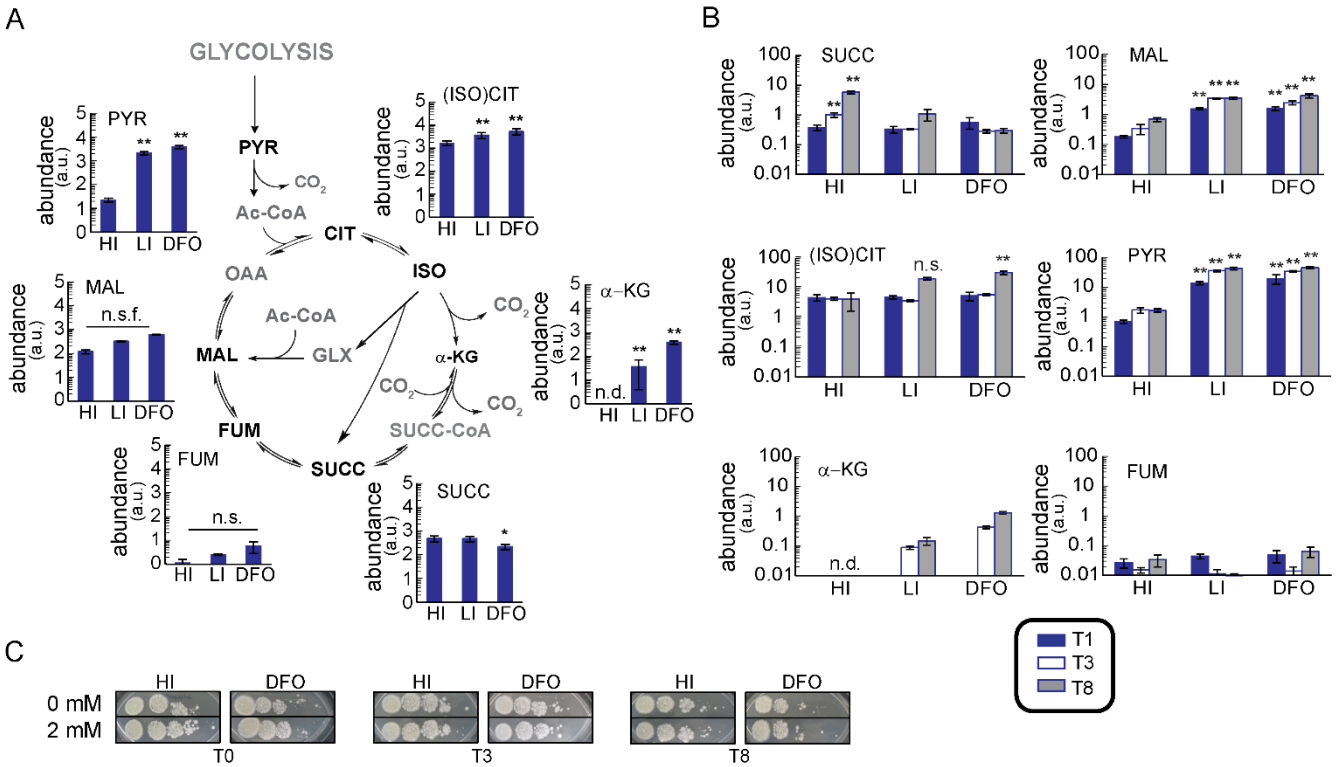

Figure 2. **Intracellular and extracellular levels of metabolites in H37Rv**. Cells were exposed to 50 µM $FeCl_3$ (HI: High Iron), 0 µM $FeCl_3$ (LI: Low Iron,) or 0 µM $FeCl_3$+ DFO (DFO). The analyzed metabolites are shown in black in the schematic pathways. A) Intracellular polar metabolites levels at 8 days. B) Extracellular polar metabolites levels at 1, 3 and 8 days. The plots show the normalized levels of metabolites. The data represent the average and the standard deviation of four biological replicates from an independent experiment, representative of two independent experiments. An arbitrary unit is reported on the y axis. The y axis is in Log10 scale and the numbers from 0 to 5 (panel A) indicate the exponent. C) Viability of H37Rv from one independent experiment. Cells were grown in liquid medium in HI and DFO conditions and in the presence of 2 mM of succinate. Aliquots of cells were collected after 0, 3 and 8 days and diluted to same final OD_{600}; 5 µL of 10-fold serial dilutions were plated on 7H10. Growth was recorded after 19-25 days.

The p-values were calculated against the HI condition and independently for the two experiments, the highest p-value was reported. n.s.f.= non-significant fold change, the observed trend change was different between independent experiments; n.s.= non-significant, p value >0.05; n.d.= non-detected; * =p value <0.05; ** =p value <0.01.

Ac-CoA: acetyl-CoA; CIT: citrate; FUM: fumarate; α-KG: α-ketoglutarate; ISO: isocitrate; (ISO)CIT: isocitrate and citrate; MAL: malate; OAA: oxaloacetate; PYR: pyruvate; SUCC: succinate; SUCC-CoA: succinyl-CoA.

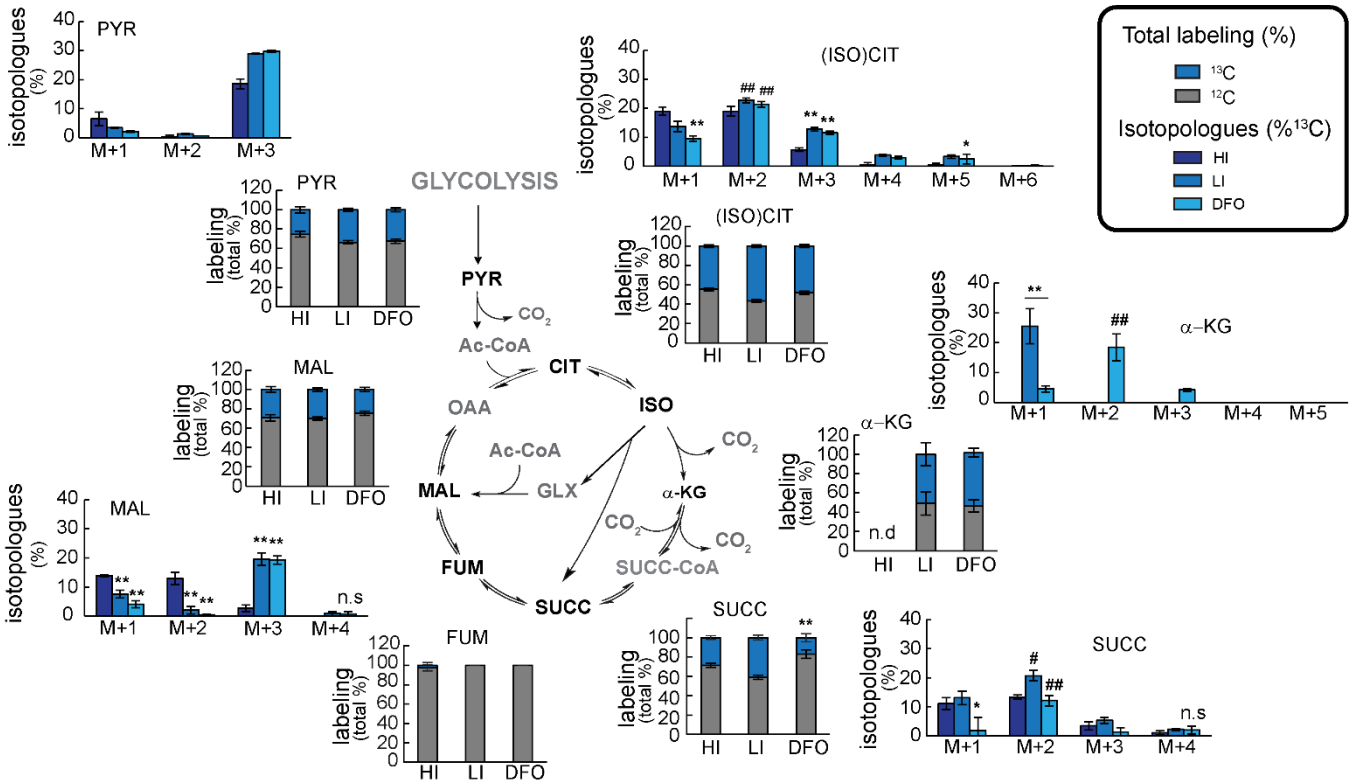

Figure 3. Percentage of labeled (^{13}C) and unlabeled (^{12}C) metabolites in H37Rv. Metabolites were extracted from cells fed with $^{13}C_3$-glycerol for 8 days in 50 µM $FeCl_3$ (HI: High Iron), 0 µM $FeCl_3$ (LI: Low Iron) or 0 µM $FeCl_3$+ DFO (DFO). The analyzed metabolites are shown in black in the schematic pathways. For each metabolite, but fumarate, two plots are shown. The stacked column plot shows the total percentage of labeled and unlabeled molecules per each metabolite pool; the clustered column plot shows the abundance in percentage of each isotopologue. The data represent the average and the standard deviation of four biological replicates from an independent experiment, representative of two independent experiments. The p-values were calculated independently for the two experiments and the highest p-value was reported. DFO/LI vs HI condition: * = p value<0.05; ** = p value <0.01; n.s.= non-significant. n.d.= non-detected. M2 vs M1: # = p value<0.05; ## = p value<0.01.

Ac-CoA: acetyl-CoA; CIT: citrate; FUM: fumarate; α-KG: α-ketoglutarate; ISO: isocitrate; (ISO)CIT: isocitrate and citrate; MAL: malate; OAA: oxaloacetate; PYR: pyruvate; SUCC: succinate; SUCC-CoA: succinyl-CoA.

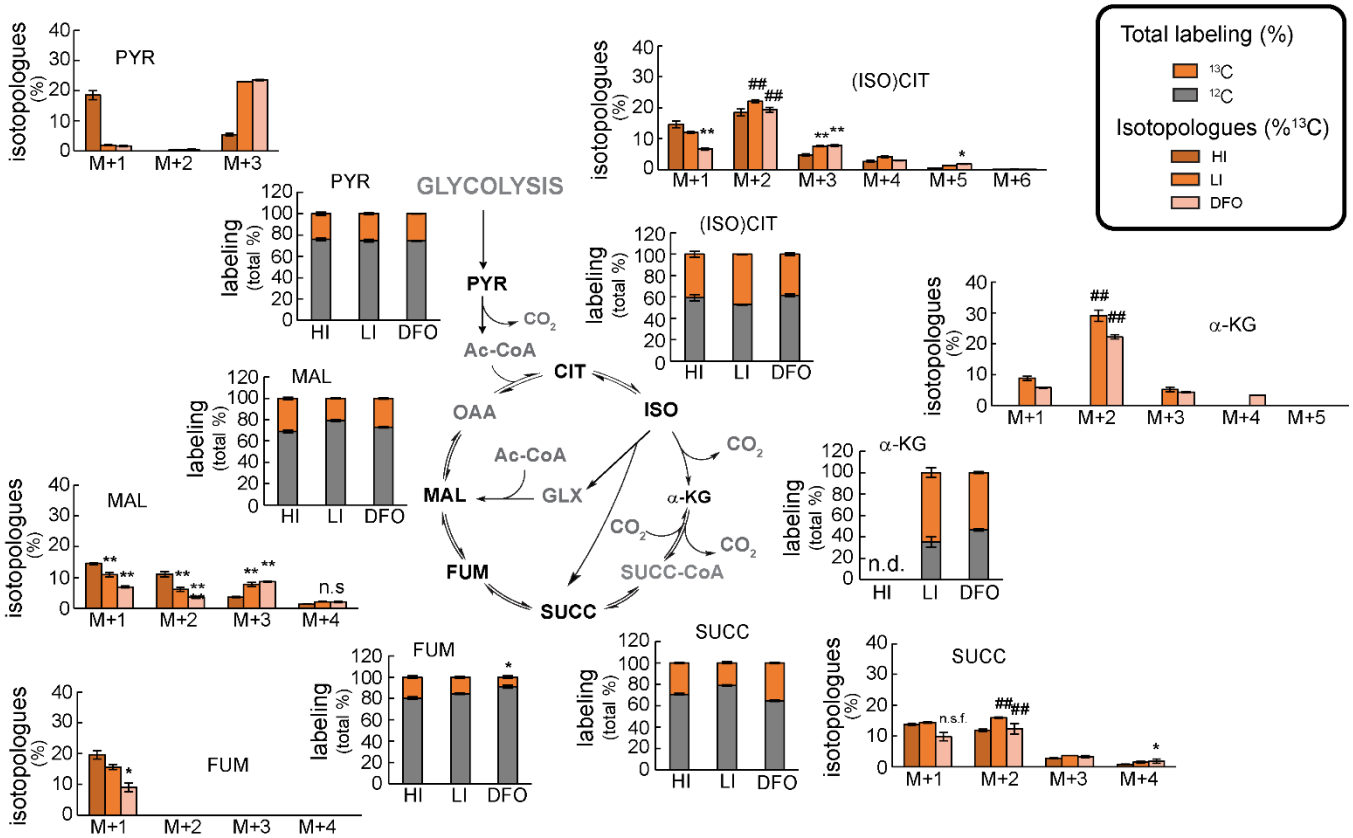

Figure 4. Percentage of labeled (^{13}C) and unlabeled (^{12}C) metabolites in the Erdman strain. Metabolites were extracted from cells fed with $^{13}C_3$-glycerol for 8 days in 50 μM $FeCl_3$ (HI: High Iron), 0 μM $FeCl_3$ (LI: Low Iron) or 0 μM $FeCl_3$+ DFO (DFO). The analyzed metabolites are shown in black in the schematic pathways. For each metabolite two plots are shown. The stacked column plots show the total percentage of labeled and unlabeled molecules per each metabolite pool; the clustered column plots show the abundance in percentage of each isotopologue. The data represent the average and the standard deviation of four biological replicates from an independent experiment, representative of four independent experiments (only two for LI condition). The p-values were calculated independently between experiments and the highest value is reported. DFO/LI vs HI: ** = p value <0.01; n.s.= non-significant; n.s.f.= non-significant fold change, the observed trend change was different between independent experiments. n.d.= non-detected. M2 vs M1: ## = p value <0.01. Ac-CoA: acetyl-CoA; CIT: citrate; FUM: fumarate; α-KG: α-ketoglutarate; ISO: isocitrate; (ISO)CIT: isocitrate and citrate; MAL: malate; OAA: oxaloacetate; PYR: pyruvate¸ SUCC: succinate; SUCC-CoA: succinyl-CoA.

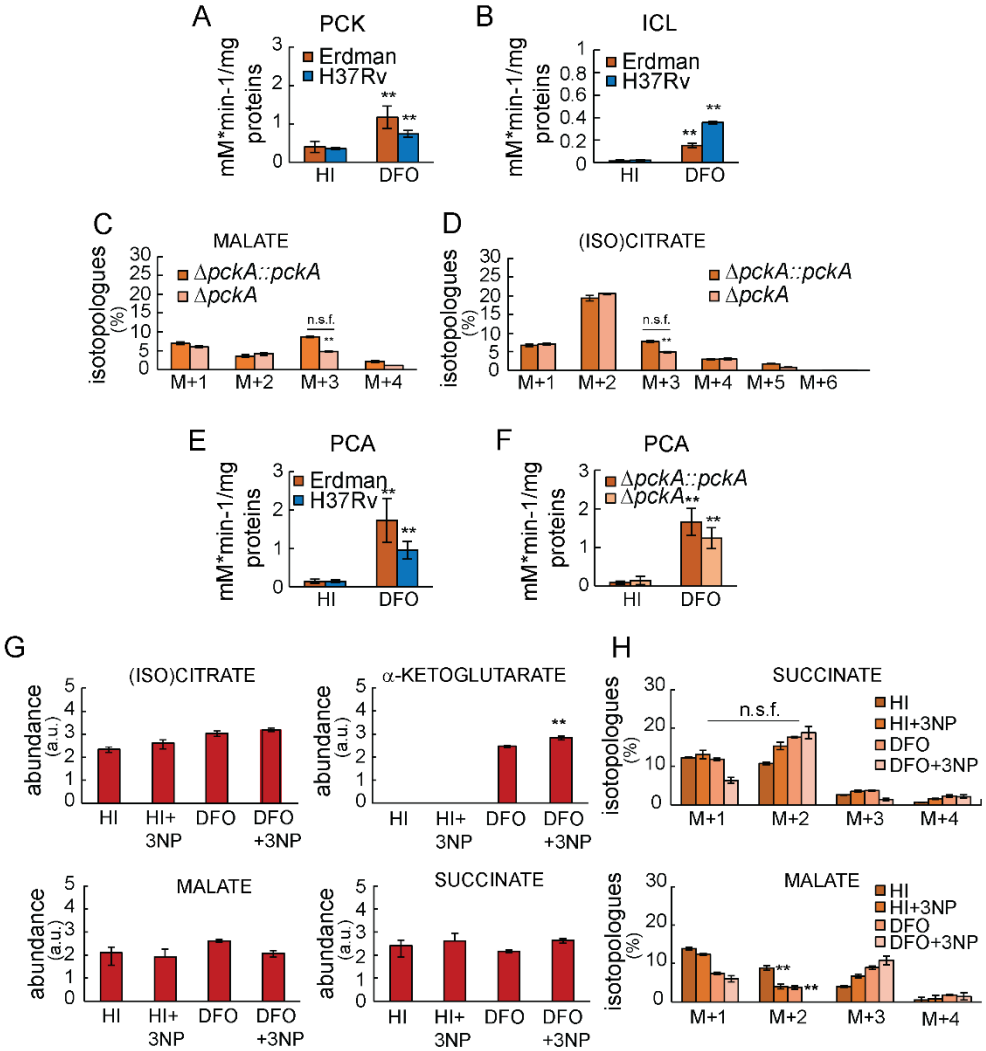

Figure 5. **Analysis of iron-independent metabolic routes**. Cells were exposed to 50 μM $FeCl_3$ (HI), or 0 μM $FeCl_3$+ DFO (DFO). A) Enzymatic activity of phosphoenolpyruvate carboxykinase (PCK), reaction from phosphoenolpyruvate to oxaloacetate; B) Enzymatic activity of isocitrate lyase (ICL); the plots show the activity in (mM of NADH × min^{-1})/mg of total protein detected in cell-free extracts after 3 days of exposure to DFO or HI condition. Data show average and standard deviation from two (H37Rv) or three (Erdman strain) independent experiments and two technical replicates each (A) or from one independent experiment and three technical replicates (B). C, D) Isotopologue distribution of intracellular malate (C) and isocitrate (D) in Erdman-derived Δ*pckA::pckA* and Δ*pckA* strains after 8 days of exposure to DFO or HI conditions and fed with $^{13}C_3$-glycerol. The plots show the abundance in percentage of each isotopologue. The histograms represent average and standard deviation from four biological replicates from one experiment, representative of three independent experiments. E, F) Enzymatic activity of pyruvate carboxylase (PCA), reaction from pyruvate to oxaloacetate; the plots show the activity in (mM of NADH × min^{-1})/mg of total protein detected in cell-free extracts after 3 days

Continued on the next page …

… continued from Figure 5

of exposure to DFO or HI condition. Data show average and standard deviation from three independent experiments and two technical replicates each. G, H) Erdman strain cells were exposed to HI or DFO condition for 8 days with or without 200 μM of inhibitor 3-nitropropionate (3NP) and fed with $^{13}C_3$-glycerol. (G) The plots show the normalized levels of metabolites; an arbitrary unit is reported on the y axis; the y axis is in Log10 scale and the numbers from 0 to 5 indicate the exponent. (H) The plots show the isotopologue distribution in percent abundance. The data represent the average and the standard deviation of four biological replicates from an independent experiment, representative of two independent experiments. The p-values were calculated independently between experiments and the highest value is reported. The p-values were calculated as follows. DFO vs HI for A, B, E, F; HI+3NP vs HI and DFO+3NP vs DFO for H; mutant vs complemented for C, D. n.s.f. = non-significant fold change, the observed trend change was different between independent experiments. ** = p value <0.01.

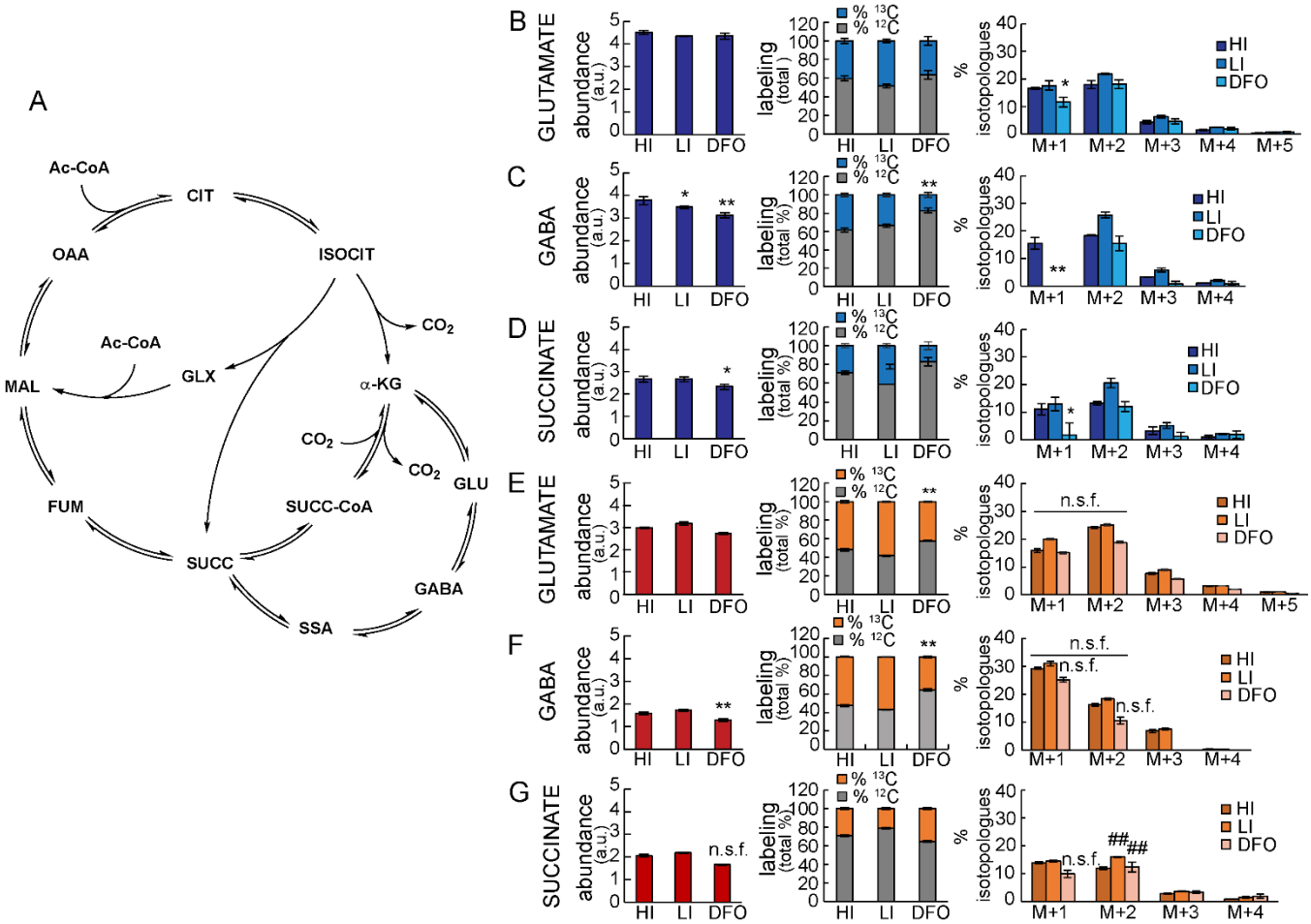

Figure 6. Analysis of GABA shunt metabolites in H37RV and Erdman strains. Cells were exposed to 50 μM $FeCl_3$ (HI: High Iron), 0 μM $FeCl_3$ (LI: Low Iron,) or 0 μM $FeCl_3$+ DFO (DFO), and fed with $^{13}C_3$-glycerol for 8 days. A) Schematic representation of the GABA shunt and the Krebs cycle. B, C, D) H37Rv; E, F, G) Erdman strain. B, E) glutamate; C, F) gamma-aminobutyric acid (GABA); D, G) succinate. Plots with one color-filled histograms represent the normalized levels of metabolites in Log_{10} scale, the numbers from 0 to 5 on the y axis indicate the exponent; plots with two color-stacked histograms represent the total abundance in percentage of labeled and unlabeled metabolite pools; plots with clustered histograms represent the abundance in percentage of each isotopologue. H37Rv data are from one experiment representative of two independent experiments and four biological replicates each; Erdman-derived strain data are from one experiment representative of four independent experiments (only two of them for the LI condition) and four biological replicates each. The histograms show average and standard deviation of four biological replicates from an independent experiment. The p-values were calculated against the HI condition; the highest p-value from the two independent experiments is shown. The differences between M+1 and M+2

Continued on the next page …

… continued from Figure 6

isotopologues in the Erdman strain (E, F) are not significant between the three experiments, the trend varied between independent experiments.

a.u.: arbitrary unit (see methods paragraph). n.s.f.= non-significant fold change, the observed trend change was different between independent experiments.

DFO vs HI or LI vs HI: * =p value <0.05; ** =p value <0.01; “n.s.f.” above the individual M+1 and M+2 bars of succinate and GABA.

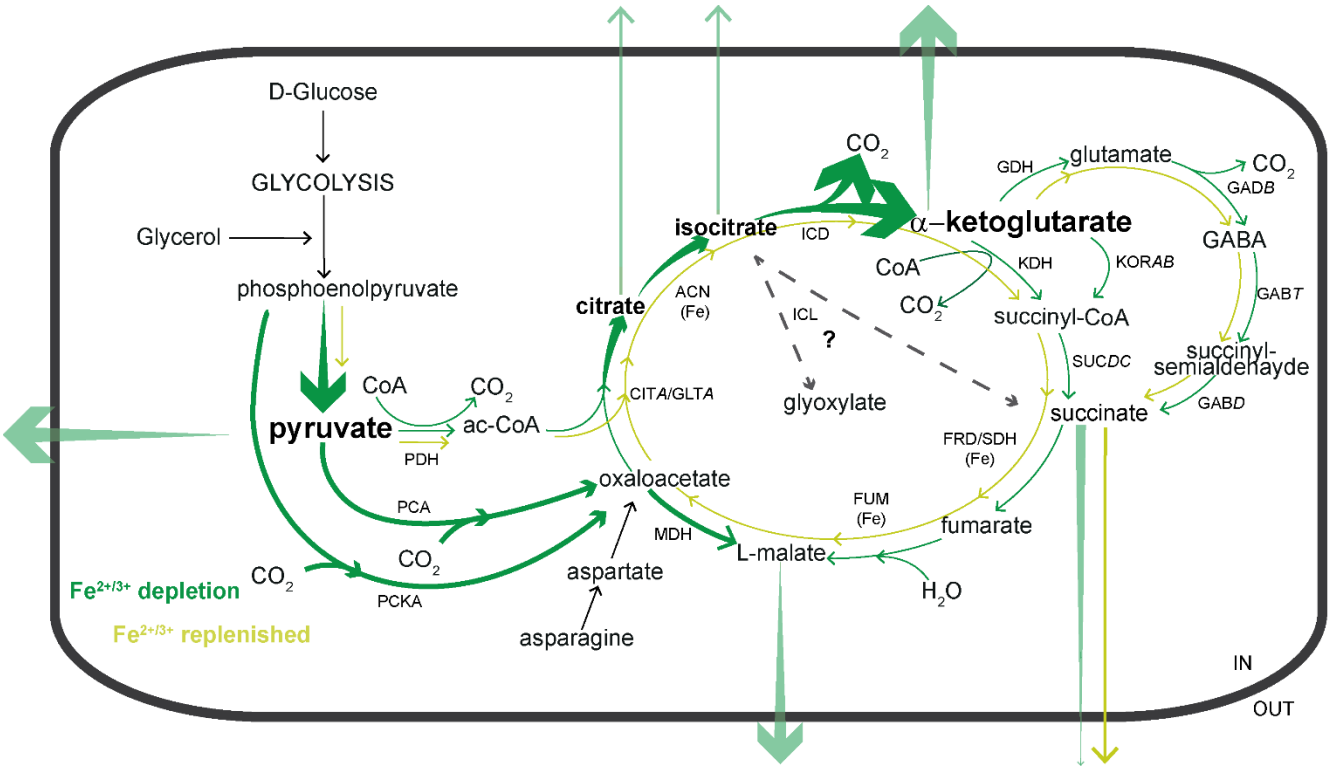

Figure 7. **Re-modeling of CCM under iron starvation in *Mtb***. The picture depicts a schematic representation of the CCM pathways active in *Mtb* exposed to Fe^{3+} deprivation in the presence of D-glucose and glycerol as carbon sources and asparagine as sole nitrogen source. The thickening arrows indicate the increase of levels of the metabolite, thicker arrows indicate a preferred route. Bold and larger font indicates accumulated metabolites. Under iron starvation, the pool of iron-dependent enzymes (denoted by Fe in parentheses in the figure) contains a reduced number of fully active molecules, which then slows the carbon flux through the Krebs cycle. The reduction in the transcript levels of iron-independent enzymes of the CCM pathways is likely a consequence of this. The disparity in efficiency between iron-dependent and iron-independent enzyme pools gives rise to the accumulation of (iso)citrate, pyruvate, and α-ketoglutarate. *Mtb* responds to these accumulations by expelling these metabolites from the cell and splitting the carbon flux from PEP/pyruvate (via PCK, PCA, and PDH activities) into both oxidative and reductive branches of the Krebs cycle. Both fluxes terminate in malate synthesis, which is then secreted. To maintain malate synthesis by succinate oxidation *Mtb* limits its secretion. Malate secretion relieves the slowdown of carbon flux through the oxidative branch of Krebs cycle. PCK and PCA anaplerotic reactions control pyruvate levels and recycle carbon dioxide stoichiometric to the α-ketoglutarate accumulation.

GDH: glutamate dehydrogenase. GAD*B*: glutamate decarboxylase. GAB*T*: 4-aminobutyrate aminotransferase. GAB*D*: succinate-semialdehyde dehydrogenase. For the other enzyme acronyms see main text.

Supporting Information

Mycobacterium tuberculosis partitions the Krebs cycle to persist under iron starvation.

Agnese Serafini[a,1], Acely Garza-Garcia[b], Davide Sorze[a], Luiz Pedro Sorio de Carvalho[b,c], and Riccardo Manganelli[a].

[a]Department of Molecular Medicine, University of Padova, Via A. Gabelli 63, Padova 35121, Italy.

[b]Mycobacterial Metabolism and Antibiotic Research Laboratory, The Francis Crick Institute, 1 Midland Rd, London NW1 1AT, UK.

[c]Chemistry Department, The Herbert Wertheim UF Scripps Institute for Biomedical Innovation & Technology, 120 Scripps Way, Jupiter, FL 33458, USA.

Agnese Serafini
Email: agnese.serafini@unipd.it

Other supporting materials for this manuscript include the following:

Dataset S1

Extended Results

Section I. *Intracellular and extracellular levels and isotopic distribution analysis of metabolites in LI vs DFO conditions.*

Few differences were detected between LI and DFO conditions. Unlike DFO, succinate levels do not decrease under LI in both H37Rv and Erdman (**Figure 2A and Figure 2–figure supplement 1A**), and (iso)citrate levels do not increase in LI in Erdman strain.

In H37Rv, total labeling analysis shows that labeled succinate levels were similar between LI and HI conditions (**Figure 3**), while they decreased in DFO, suggesting an alternative route for succinate production under LI. The isotopologue distribution of α-ketoglutarate and succinate in LI show differences compared to DFO in H37Rv (**Figure 3**). Succinate isotopologue distribution in LI (**Figure 3**) resemble (iso)citrate, with M+2 more abundant than M+1, whereas α-ketoglutarate as has only M+1 (**Figure 3**). This suggests that the glyoxylate shunt may be a dominant route only in LI. However, the lack of changes in the intracellular levels (**Figure 2)** and labeling **and (Figure 2 and 3-figure supplement 2D** and data not shown) of (iso)citrate, malate and succinate in the Δ*icl1* strain and its complemented strain supports the hypothesis that the glyoxylate shunt is not important under Fe^{3+} starvation. It is possible that in LI compared to DFO: i) α-ketoglutarate may be subject to a different metabolic circuit, and that ii) succinate originates from another route. The GABA shunt may represent this alternative route **(Figure 5A and main text**), which metabolites appear not to be significantly altered under Fe^{3+} starvation (**Figure 5B, E and F**). Like in DFO, M+1 GABA lacks in LI condition (**Figure 5C**). Overall, the minimal differences observed between LI and DFO conditions suggest that the main metabolic alterations observed in this study are directly attributable to Fe^{3+} starvation, rather than being secondary effects of growth cessation or unspecific DFO effect.

Section II. *Fumarate synthesis*

The ^{13}C isotopic profile of fumarate does not align with that of succinate and malate (**Figure 4H and L**), despite the clear indication that the M+2 malate is derived from succinate (**Figure 5H**) and that the fumarate route is obligate. The fumarate pool has only the M+1 isotopologue. An explanation for these results may derive from the intracellular localization of the enzymatic complexes involved in the synthesis of malate. Given that succinate dehydrogenase is cell-membrane embedded, it seems reasonable to think that the other enzymes involved in the synthesis and oxidation of succinate are also localized close to the membrane. In this scenario, the succinate-derived fumarate might be immediately transformed to fumarate and difficult to detect. Therefore, the only presence of M+1 isotopologue reveals the activity of an alternative metabolic route whose enzymes are likely localized in a separated area of the bacterial cell. Fumarate is also the degradation product of arginosuccinate via ArgH/Rv1659 lyase (Paul et al. 2013) in the arginine succinate biosynthetic pathway. The entire *Arg* operon

is upregulated under Fe^{3+} starvation (Kurthkoti et al. 2017) and our metabolic analysis showed a reduction of M+1 fumarate abundance under Fe^{3+} starvation. The reduction of labeling may represent a symptom of the general reduced cellular metabolism under Fe^{3+} depletion and the upregulation of the pathway a tentative to maintain free fumarate pool size sufficient for cell homeostasis.

The presence of only the M+1 fumarate isotopologue, even in the presence of sufficient Fe^{3+}, suggests that the specific growth medium used affects the fumarate metabolism. Our previous work (Serafini et al. 2019) demonstrated a clear overlap between the isotopic profiles of fumarate, malate and succinate in cells grown in a media with different composition of C and N sources. The reasons for these differences related to the growth media used remain unclear.

Section III. *Oxaloacetate*

Aspartate is usually used as a proxy for oxaloacetate analysis. However, in our experimental conditions, asparagine (38 mM) is present in the medium, feeding the intracellular aspartate pool. This results in a consistent amount of unlabeled Asn-derived oxaloacetate entering the Krebs cycle, and therefore aspartate cannot be used to track carbon flux. The reduced labeling percentage of aspartate (below 5%, data not shown) compared to the other Krebs cycle intermediates confirms that. The consistent amount of unlabeled Asn-derived oxaloacetate explains the prevalence of M+1 and M+2 isotopologues in (iso)citrate, α-ketoglutarate and succinate which is likely due to PDH activity (**Figure 3 and 4–figure supplement 1A-C**).

Section IV. *Comparison of theoretical scenarios from* **Figure 3 and 4–figure supplement 1***D-S with labeling results*.

Only the scenarios illustrated in the **Figure 3 and 4–figure supplement 1D, E, P and Q** lead to the production of M+3 malate. Despite producing M+3 malate, the **Figure 3 and 4–figure supplement 1D** scenario also produces M+5 isocitrate and M+4 succinate, which show low abundance in our measurements (**Figure 3 and 4**), suggesting that additional route/s contributes to the generation of M+3 malate. Importantly, this scenario employs two labeled acetyl-CoA molecules. Since the abundance of labeled pyruvate, the precursor of labeled acetyl-CoA, is well below 50% of the total pyruvate (**Figure 3 and 4**), this scenario is unlikely.

The **Figure 3 and 4–figure supplement 1E** scenario produces M+3 malate, M+2 succinate and M+3 (iso)citrate. M+2 succinate is significantly abundant in HI and DFO (**Figure 3 and 4**), whereas M+3 (iso)citrate increases in DFO condition (**Figure 3 and 4**) suggesting that this last isotopologue can derive from PCK-derived oxaloacetate. The **Figure 3 and 4–figure supplement 1E** scenario employs one labeled acetyl-CoA that is used by malate synthase (GlcB), similarly to **Figure 3 and 4–figure supplement 1F** scenario that employs one labeled acetyl-CoA but that is used by citrate synthase (GltA). S4F produces M+1 malate, which abundance decreases in DFO, M+5 (iso)citrate and M+4 succinate, which are the least abundant isotopologues of (iso)citrate and succinate and, their abundance slightly increases in DFO (**Figure. 3 and 4**). Additionally, the isotopologues

produced in the **Figure 3 and 4–figure supplement 1F** combination in DFO are less abundant in our experimental data compared to those produced in the **Figure 3 and 4–figure supplement 1E** combination.

The **Figure 3 and 4–figure supplement 1P** scenario yields M+3 malate, M+2 succinate and M+3 (iso)citrate, however it derives from the combination of two labeled acetyl-CoA, making it as unlikely as the **Figure 3 and 4–figure supplement 1D** scenario.

Finally, the **Figure 3 and 4–figure supplement 1Q** scenario produces M+1 (iso)citrate, together with M+3 malate. This scenario includes one labeled acetyl-CoA that is used by GlcB, similarly to **Figure 3 and 4–figure supplement 1R** scenario that employs one labeled acetyl-CoA but that is used by citrate synthase (GltA). The probability of the **Figure 3 and 4–figure supplement 1Q** scenario should be equivalent to that of the **Figure 3 and 4–figure supplement 1R** scenario. The latter produces M+1 malate, M+2 succinate and M+3 (iso)citrate. Both **Figure 3 and 4–figure supplement 1Q** and **Figure 3 and 4–figure supplement 1R** produce specific isotopologues whose changes in abundance in the DFO condition compared to the HI condition show opposite directions (**Figure 3 and 4**).

In summary, while the four theoretical scenarios that include the glyoxylate cycle described above reflect qualitatively our labeling results, several quantitative discrepancies exist with the measured and predicted abundances of the isotopologues. These observations do not explain the increased abundance of M+3 malate consistently observed under Fe^{3+} starvation and raise doubts about the relevance of glyoxylate shunt under Fe^{3+} starvation.

References

Paul A, Mishra A, Surolia A, Vijayan M. 2013. Cloning, expression, purification, crystallization and preliminary X-ray studies of argininosuccinate lyase (Rv1659) from *Mycobacterium tuberculosis*. *Acta Crystallogr Sect F Struct Biol Cryst Commun* **69**: 1422-1424. DOI: 10.1107/S1744309113031138, PMID: 24316845

Kurthkoti K, Amin H, Marakalala MJ, Ghanny S, Subbian S, Sakatos A, Livny J, Fortune SM, Berney M, Rodriguez GM. 2017. The capacity of *Mycobacterium tuberculosis* to survive iron starvation might enable it to persist in iron-deprived microenvironments of human granulomas. *mBio* Aug **8**(4):e01092-17. DOI: 10.1128/mBio.01092-17, PMID: 28811344.

Serafini A, Tan L, Horswell S, Howell S, Greenwood DJ, Hunt DM, Phan MD, Schembri M, Monteleone M, Montague CR, Britton W, Garza-Garcia A, Snijders AP, VanderVen B, Gutierrez MG, West NP, de Carvalho LPS. 2019. *Mycobacterium tuberculosis* requires glyoxylate shunt and reverse methylcitrate cycle for lactate and pyruvate metabolism. *Mol Microbiol* **112**: 1284-1307. DOI: 10.1111/mmi.14362, PMID: 31389636

Supplementary Figures

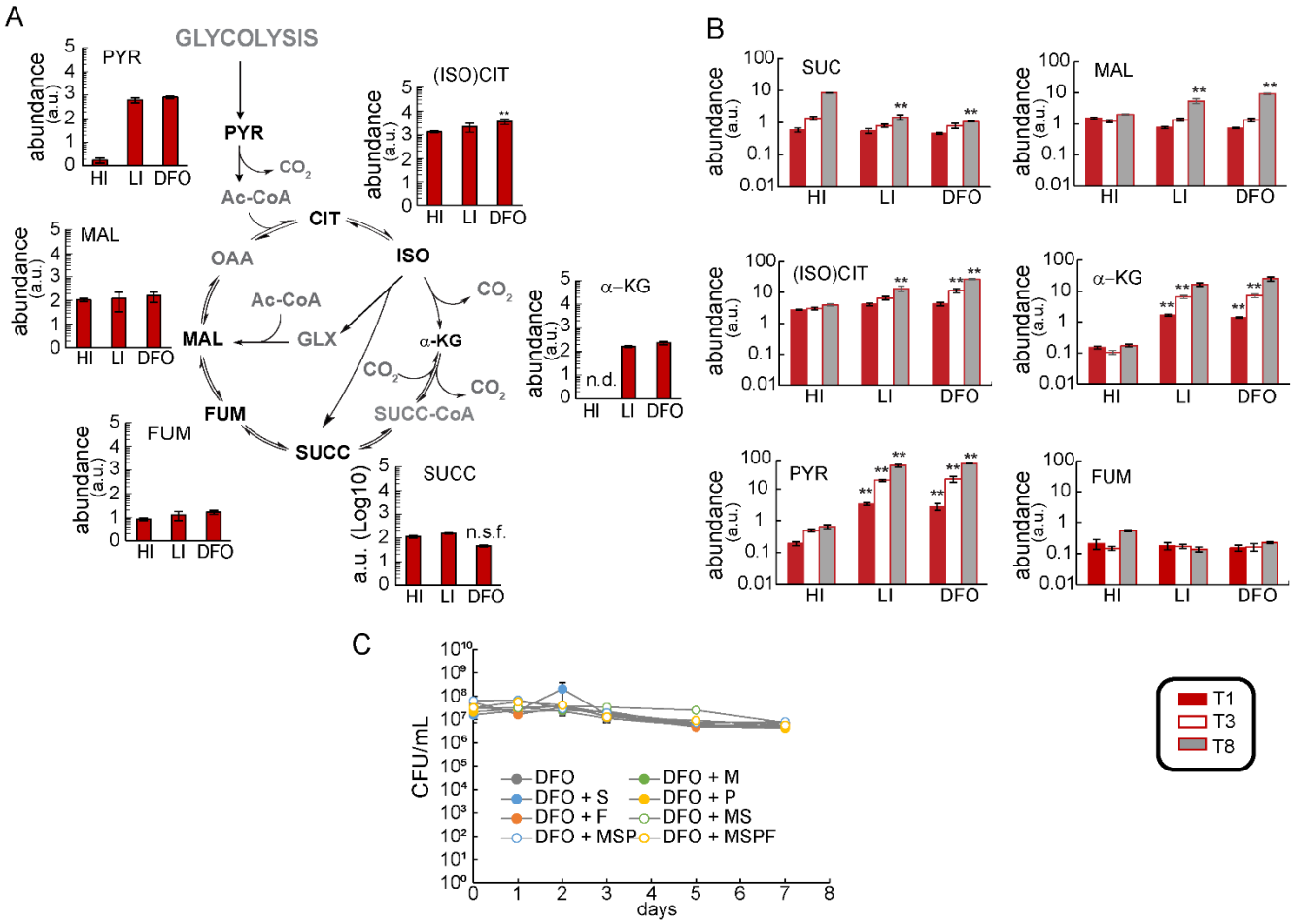

Figure 2 - figure supplement 1.

Intracellular and extracellular levels of metabolites in the Erdman strain. Cells were exposed to 50 μM $FeCl_3$ (HI: High Iron), 0 μM $FeCl_3$ (LI: Low Iron,) or 0 μM $FeCl_3$+ DFO (DFO). The analyzed metabolites are shown in black in the schematic pathways. A) Intracellular polar metabolites levels at 8 days. The slight decrease in succinate levels (0.66 FC) was not observed in the other four independent experiments in which no changes were observed in LI and DFO conditions compared to HI condition. B) Extracellular polar metabolites levels at 1,3 and 8 days. The plots show the normalized levels of metabolites. The data represent the average and the standard deviation of four biological replicates from an independent experiment, representative of four independent experiments for the HI and DFO conditions, and two independent experiments for the LI condition. An arbitrary unit is reported on the y axis. The y axis is in Log_{10} scale and the numbers from 0 to 5 (panel A) indicate the exponent. G) Viability of cells exposed to DFO in the presence of 2 mM of malate (DFO+M), succinate (DFO+S), pyruvate (DFO+P) or a combination of the three (DFO+M+S+P). The plot reports the viability measured as CFU/mL in Log_{10} scale. The data are representative of one independent experiment (average and average deviation of two technical replicates).

The p-values were calculated against the HI condition and independently for the four experiments; the highest p-value is reported. * = p value < 0.05; ** = p value <0.01. n.d. = not detected. n.s.f. = not significant fold change, the observed trend change was different between independent experiments.

Ac-CoA: acetyl-CoA; CIT: citrate; FUM: fumarate; α-KG: α-ketoglutarate; ISO: isocitrate; (ISO)CIT: isocitrate and citrate; MAL: malate; OAA: oxaloacetate; PYR: pyruvate SUCC: succinate; SUCC-CoA: succinyl-CoA.

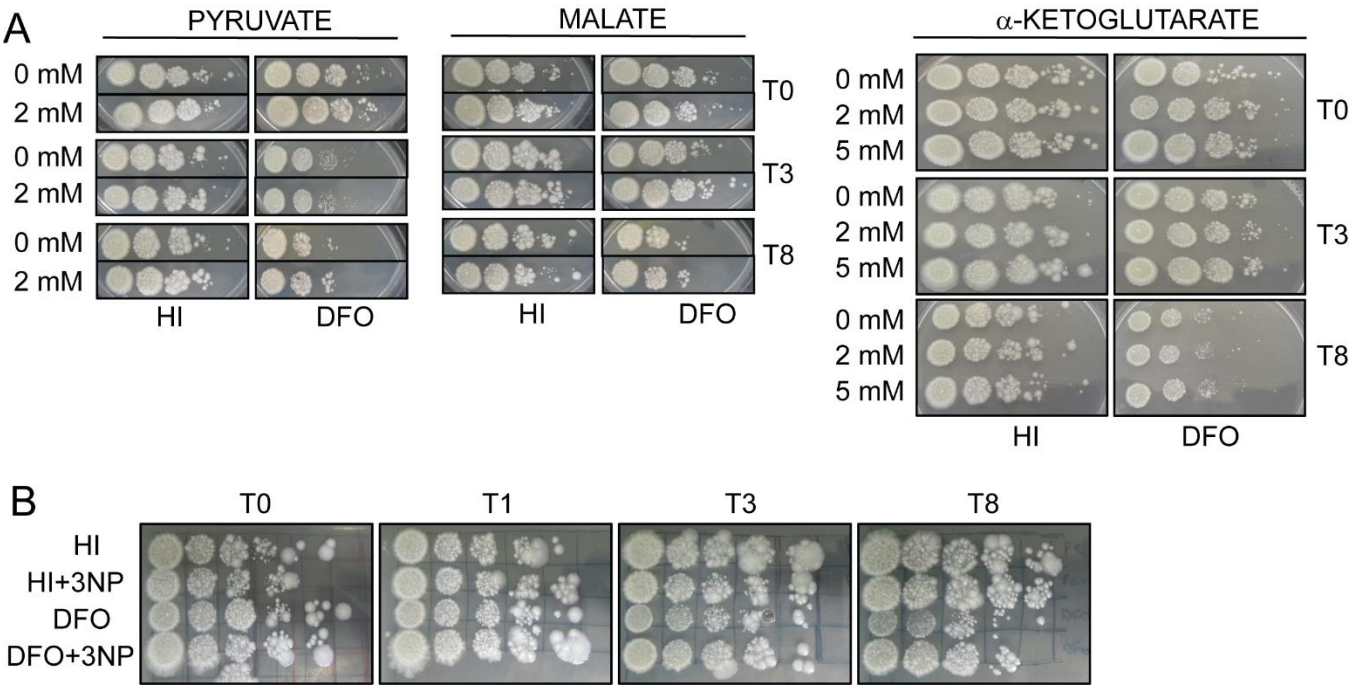

Figure 2 - figure supplement 2.

Viability of *Mtb* exposed to severe Fe^{3+} starvation and in the presence of 2 mM or 5 mM Krebs cycle intermediates (A, H37Rv) or 200 µM 3NP (B, Erdman). Cells were exposed to 50 µM $FeCl_3$ (HI: High Iron), or 0 µM $FeCl_3$+ DFO (DFO) in liquid medium for 8 days. Aliquots of cells were collected after 0, 1, 3 and 8 days, diluted to a final OD_{600} of 0.1 and 5 µL of a 10-fold serial dilution were plated on 7H10/ADC. Growth was recorded after 19-25 days.

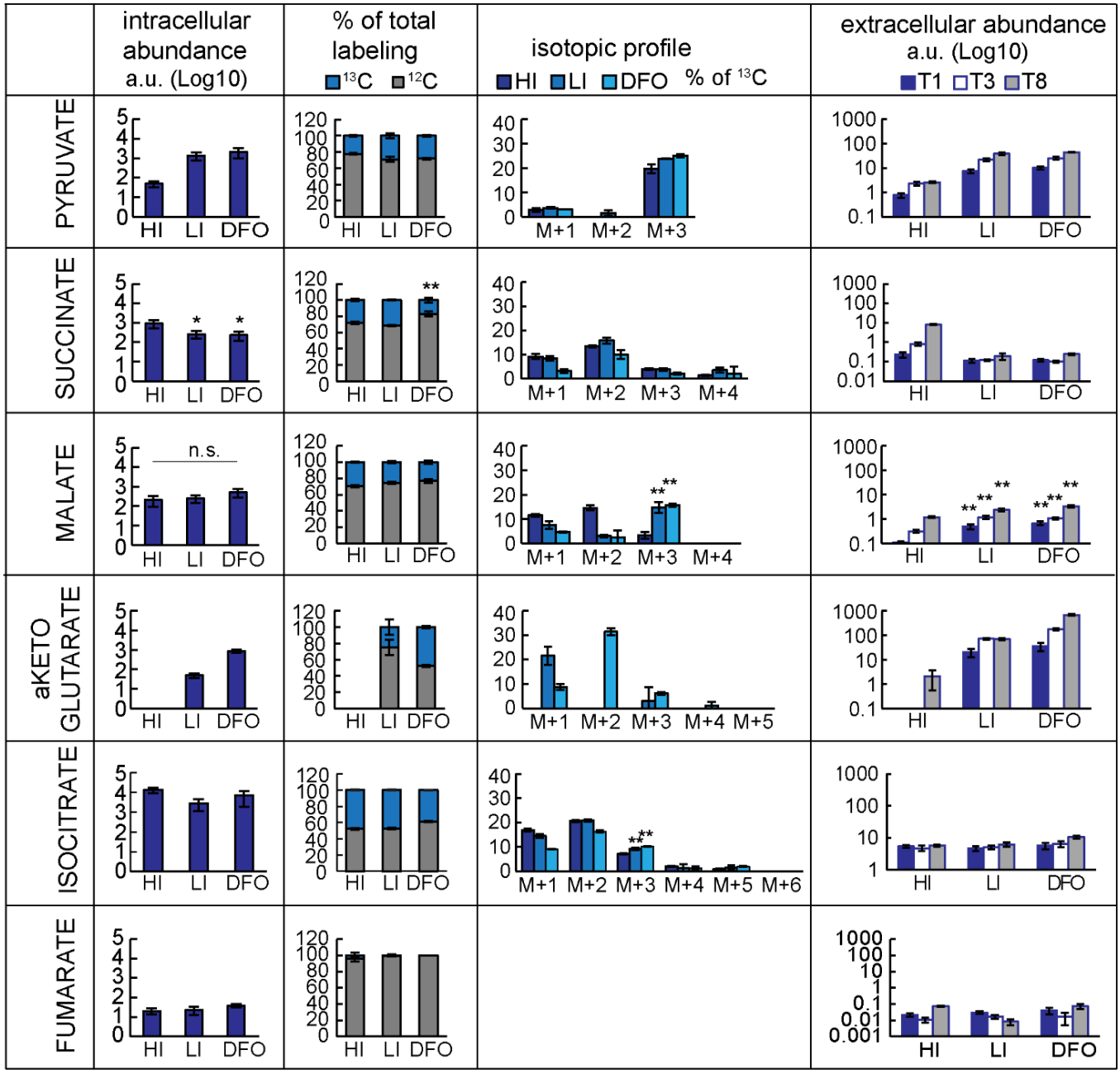

Figure 2 and 3 - figure supplement 1.

Analysis of metabolites in the H37Rv-derived Δ*icl1::icl1* complemented strain. Cells were exposed to 50 μM $FeCl_3$ (HI: High Iron), 0 μM $FeCl_3$ (LI: Low Iron,) or 0 μM $FeCl_3$+ DFO (DFO), and fed with $^{13}C_3$-glycerol. Intracellular metabolites were determined after 8 days; extracellular metabolites were determined after 1,3 and 8 days. The plots show the normalized levels of metabolites. The data represent average and standard deviation from one experiment and four biological replicates. The plots of intracellular abundance are in Log_{10} scale, the numbers from 0 to 5 on the y axis indicate the exponent. The column headers contain the labels of the y axis. The p-values were calculated against HI condition. n.s. = non-significant, p value >0.05; * = p value <0.05; ** = p value <0.01. a.u. = arbitrary unit.

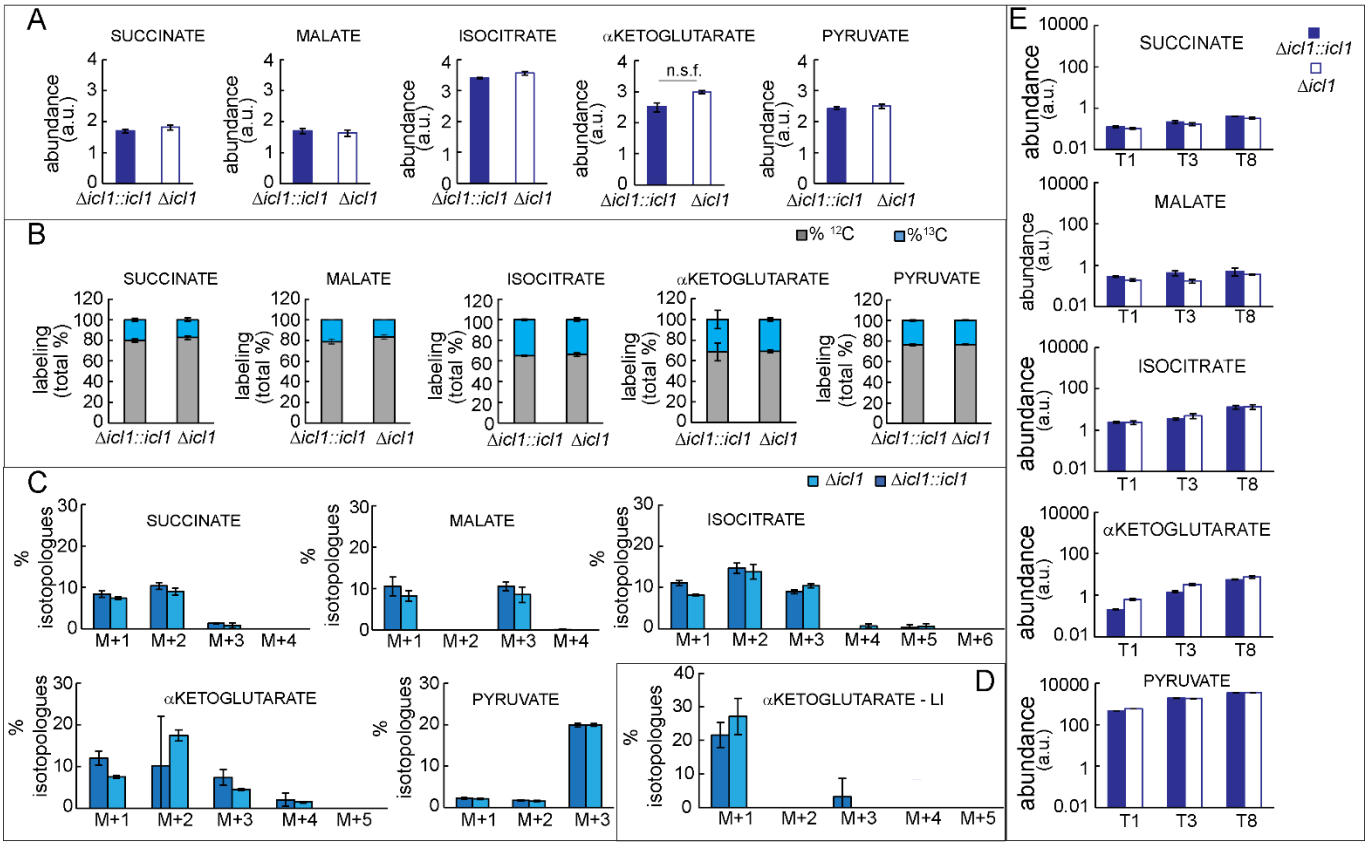

Figure 2 and 3 - figure supplement 2.

Analysis of metabolites in the H37Rv-derived *icl1* mutant (Δ*icl1*) compared to its complemented strain (Δ*icl1::icl1*) in the DFO condition. Cells were exposed to 0 µM $FeCl_3$+ DFO (DFO), and fed with $^{13}C_3$-glycerol for 8 days. Intracellular metabolites were extracte after 8 days; extracellular metabolites were extracted after 1,3 and 8 days. A) Normalized abundance of intracellular metabolites in Log_{10} scale, the numbers from 0 to 4 on the y axis indicate the exponent. An arbitrary unit is reported. B) Total percentage of labeled and unlabeled metabolites. C) Isotopologue distribution of metabolites. D) Isotopologue distribution of the α-ketoglutarate pool in the low iron (LI; 0 µM $FeCl_3$) condition. E) Normalized abundance of extracellular metabolites in Log_{10} scale. A, B, C, E: data from one experiment representative of two independent experiments and four biological replicates. D: data from one independent experiment and four biological replicates each. The data represent average and standard deviation of four biological replicates from an independent experiment. n.s.f. = not significant fold change, the observed trend change was different between independent experiments. a.u. = arbitrary unit.

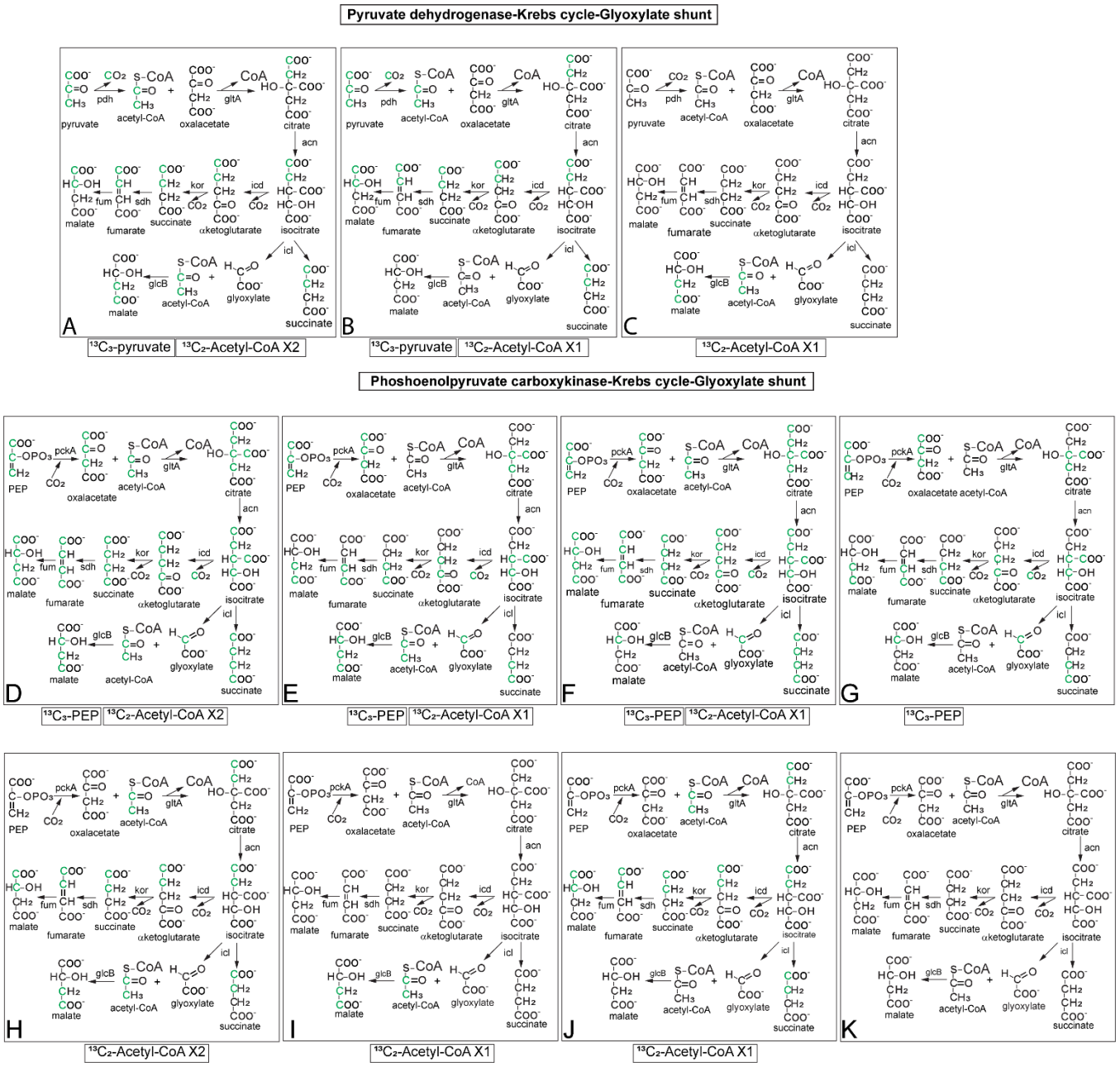

Figure 3 and 4 - figure supplement 1 continued on the next page...

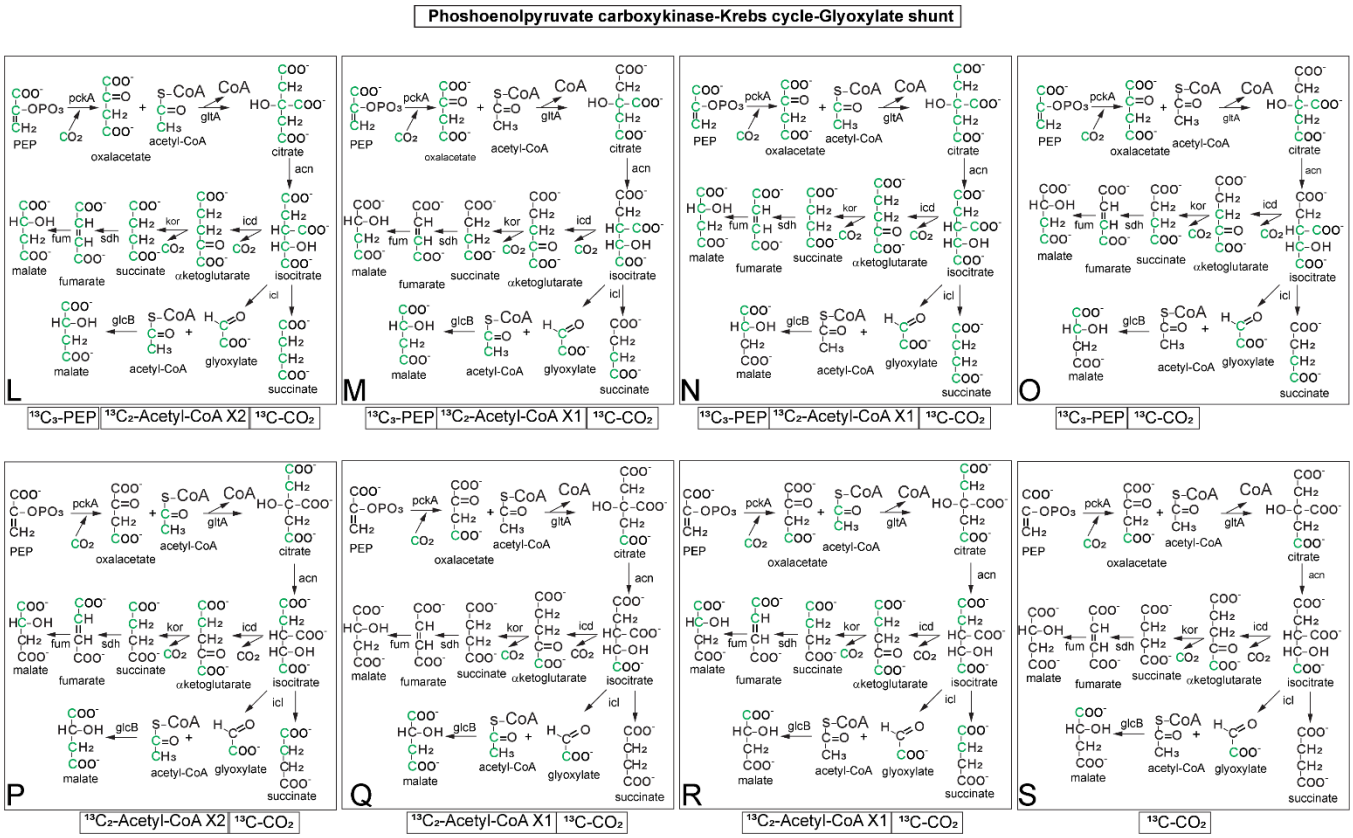

Figure 3 and 4 - figure supplement 1.

Schematic representation of ^{13}C-phosphoenolpyruvate, ^{13}C-pyruvate and ^{13}C-carbon dioxide assimilation through PDH, PCK, the Krebs cycle and the glyoxylate shunt. Atoms of ^{13}C are marked in green. The panels A-C include the activity of pyruvate dehydrogenase (PDH), the Krebs cycle and the glyoxylate shunt. The panels D-S include the activity of phosphoenolpyruvate carboxykinase (PCK), the Krebs cycle and the glyoxylate shunt. Labeled acetyl-CoA is assumed to derive from PDH activity. The bottom of each panel indicates which input metabolite is labeled. The labeling profiles of metabolites downstream to phosphoenolpyruvate (PEP) are identical if PCK is replaced by pyruvate carboxylase and PEP is replace by pyruvate. To simplify, only one of the enzymes for α-ketoglutarate degradation and citrate synthesis are reported. Acn: aconitase. GlcB: malate synthase. GltA: citrate synthase. Icd: isocitrate dehydrogenase. Icl: isocitrate lyase. Kor: αketoglutarate ferredoxin-oxidoreductase. Mdh: malate dehydrogenase. Sdh: succinate dehydrogenase.

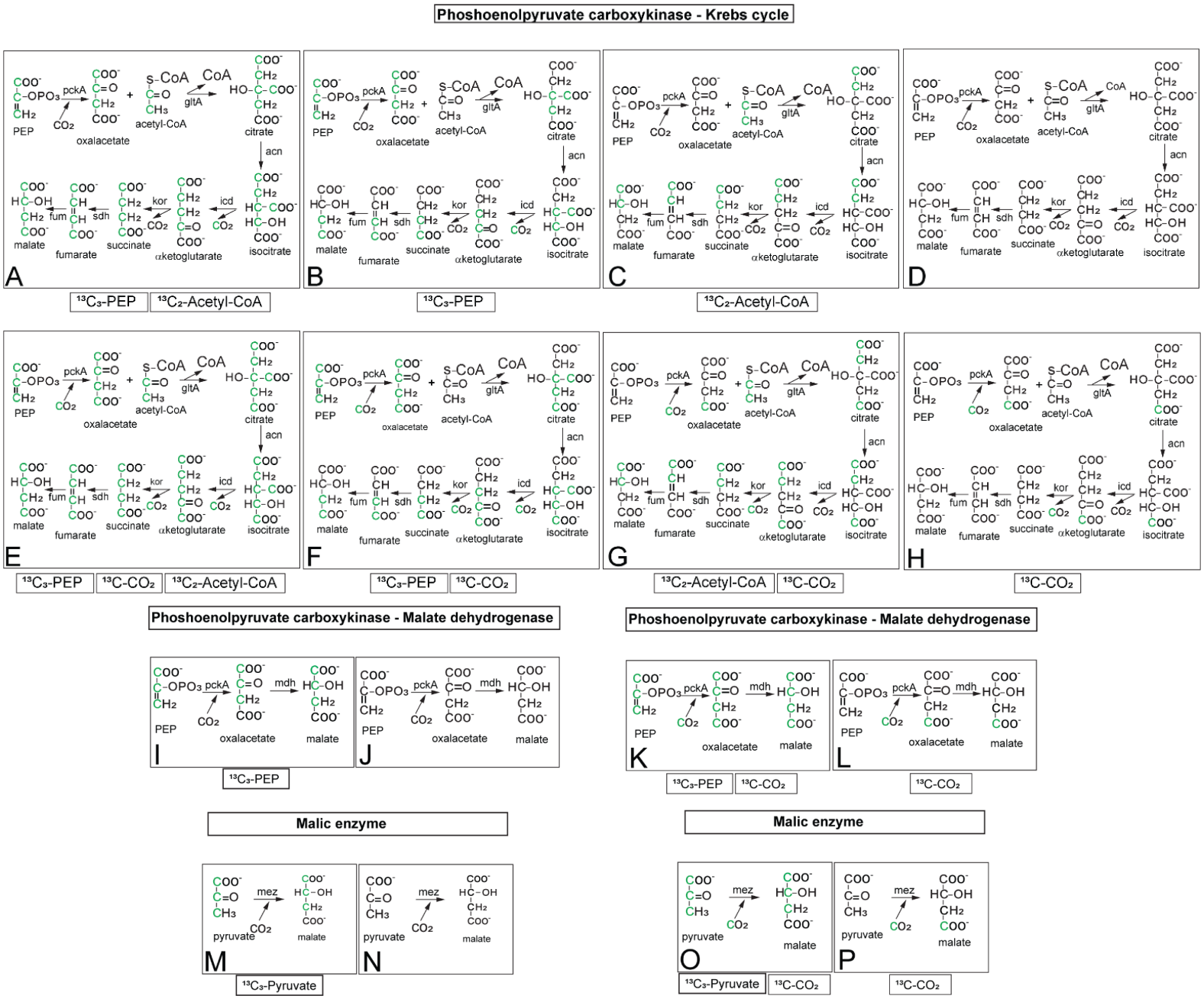

Figure 3 and 4 - figure supplement 2.

Schematic representation of ^{13}C-phosphoenolpyruvate, ^{13}C-pyruvate and ^{13}C-carbon dioxide assimilation through PCK, MEZ and the Krebs cycle. The panels A-H include the activity of phosphoenolpyruvate carboxykinase (PCK) and the Krebs cycle. Labeled acetyl-CoA is assumed to derive from PDH activity. The panels I and L include the anaplerotic reaction of PCK and the reduction of oxaloacetate to malate by MDH. The labeling profiles of metabolites downstream to phosphoenolpyruvate (PEP) are identical if PCK is replaced by pyruvate carboxylase and PEP is replaced by pyruvate (A-L). The panels M-N include the anaplerotic reaction of malic enzyme (MEZ) from pyruvate to malate. To simplify, only one of the enzymes for α-ketoglutarate degradation and citrate synthesis are reported. The bottom of each panel indicates which input metabolite is labeled.

Acn: aconitase. GltA: citrate synthase. Icd: isocitrate dehydrogenase. Kor: α-ketoglutarate oxidoreductase. Sdh: succinate dehydrogenase.